The Equilibration of Short Baroclinic Waves

Balasubramanian Govindasamy*

Program in Atmospheric and Oceanic Sciences, Princeton University, Princeton, New Jersey

S. T. Garner

Geophysical Fluid Dynamics Laboratory/NOAA, Princeton, New Jersey

(Manuscript received 12 August 1996, in final form 8 April 1997)

ABSTRACT

The life cycles of short baroclinic waves are investigated with the intention of completing a simple classification of nonlinear equilibration scenarios. Short waves become important in moist environments as latent heating reduces the scale of maximum baroclinic instability. Long-wave life cycles (wavenumber 6) were previously found to depend on details of the low-level momentum fluxes established during the earliest stages of development. These fluxes also serve as a focal point for the present study.

For a realistic, zonally symmetric jet on the sphere, the normal-mode life cycle of a short wave (wavenumber 8) under both dry and moist conditions is described. Latent heating intensifies the low pressure system and frontal zones but does not alter the broader details of the life cycle. The normal modes have predominantly equatorward momentum fluxes, in contrast to the mainly poleward momentum fluxes of long waves. The short waves are more meridionally confined. The equatorward momentum fluxes direct the waves toward cyclonic breaking. The feedback with the zonal-mean wind, the so-called barotropic governor, is less effective than in the standard long-wave life cycle, which ends in anticyclonic breaking. However, in contrast to long-wave life cycles that are "engineered" to produce equatorward momentum fluxes, relatively little potential vorticity and surface temperature anomaly roll up into isolated vortices. Therefore, the short wave undergoes protracted barotropic decay leading to complete zonalization. Short waves also have a brief period of baroclinic decay due to cold advection over the surface cyclones.

Eliassen–Palm cross sections for the short-wave life cycles show the usual combination of upward and meridional propagation of wave activity. However, the meridional propagation is mainly toward the pole and there is a consequent zonal-mean deceleration at high latitudes. These details are included in the proposed classification of equilibration scenarios.

1. Introduction

Recently, Whitaker and Snyder (1993) and Balasubramanian and Garner (1997, hereafter BG97) compared dry wavenumber 6 baroclinic life cycles in Cartesian and spherical geometry. They contrasted the "anticyclonic" behavior of spherical wavenumber 6—in which the eddies exhibit a robust SW–NE tilt and poleward momenutm flux—to the "cyclonic" behavior of the same wave in Cartesian geometry—where the eddies tilt NW–SE and the flux is equatorward. The more recent study (BG97) explained the drastic differences in terms of the interaction of the eddy momentum flux convergence with the zonal-mean flow. The sign of the meridional tilt and the strength of the feedback throughout the life cycle were both attributed to the characteristics of the linear mode. The wavenumber-6 normal-mode flux has an equatorward bias in Cartesian geometry and a slight poleward bias in spherical geometry. As a result of this difference, the zonal-mean flow alterations in the two geometries are sharply different.

Normal-mode experiments suggest that the fully equilibrated state of an inviscid baroclinic wave consists of either a zonally symmetric flow or a train of cyclonic vortices. Anticyclonic long-wave life cycles on the sphere ["LC1" of Thorncroft et al. (1993), hereafter THM] fall into the first category. Cyclonic long-wave life cycles on the sphere ("LC2" of THM) and, to a large extent, Cartesian normal modes at the same scale (BG97) belong to the second category. The same type of contrast can be seen in nature (THM) and in general circulation models (Lee and Feldstein 1996). Cyclonic long-wave development on the sphere is obtained by adding cyclonic barotropic shear across the jet in the

* Current affiliation: Climate and Integrated System Modeling, Lawrence Livermore National Laboratory, Livermore, California.

Corresponding author address: Dr. Balasubramanian Govindasamy, Climate and Integrated System Modeling, Lawrence Livermore National Laboratory, P.O. Box 808, L-256, Livermore, CA 94551-9900.
E-mail: BALA@LLNL.GOV

initial state. It was shown in BG97 that the difference in momentum fluxes in the linear stage between cyclonic and anticyclonic life cycles on the sphere is similar to the difference between spherical and Cartesian life cycles and it was argued that this difference explains the sensitivity of the equilibration to initial zonal-mean barotropic shear at wavenumber 6. The anticyclonic life cycles, with poleward momentum fluxes, undergo intense barotropic decay associated with the feedback between momentum flux convergence and the zonal-mean zonal wind—an interaction known as the ''barotropic governor'' (James 1987; Nakamura 1993). The cyclonic life cycles, with equatorward momentum fluxes, show weak decay and a relatively early shutdown of the feedback.

The studies by THM, BG97, and Whitaker and Snyder (1993) consider only wavenumber 6 and its subharmonics. Simmons and Hoskins's (1978) study of baroclinic waves on the sphere showed that short waves (wavenumber 9) exhibit time-mean *equatorward* momentum fluxes—as in LC2 and Cartesian wavenumber 6—but undergo normal barotropic decay toward a zonally symmetric final state. Thus, despite the connection between flux direction and long-term behavior at wavenumber 6, equatorward momentum flux is not a sufficient impediment to zonalization. Weak barotropic feedback alone is also insufficient to prevent zonalization: in a special experiment at wavenumber 6 in which the zonal-mean forcing by momentum fluxes was artificially suppressed, BG97 found that waves can zonalize normally despite a weak barotropic governor. They therefore speculated that a mechanism to symmetrize the nonlinear vortices was also necessary for eddy longevity. In focusing on short-wave equilibration, the present study should help to identify sufficient conditions for the creation of long-term zonal and nonzonal states.

Although long waves dominate the energy spectrum in the upper troposphere (Lee and Held 1993), short waves are an important component of the climate system. Latent heating decreases the wavelength of maximum baroclinic instablility (Gall 1976; Wang and Barcilon 1986; Emanuel et al. 1987; Joly and Thorpe 1989; Gutowski et al. 1992) and confines it more to the lower troposphere. Numerous observational investigations (Danard 1964; Tracton 1973; Gyakum 1983a,b; Davis and Emanuel 1991) and modeling studies (Fantini 1991; Montgomery and Farrell 1991; Hedley and Yau 1991; Orlanski and Katzfy 1987; Balasubramanian and Yau 1994a,b, 1996) have shown that condensation has a profound impact on the structure as well as the growth of individual vortices. To the extent that normal-mode results describe more realistic disturbances, explaining the dependence of life cycle behavior on zonal scale can be crucial for an understanding of observed variability in storm tracks (Nakamura 1992).

In Balasubramanian and Yau (1994b, 1996) water vapor and liquid water were both predicted. The initial condition consisted of a finite-amplitude perturbation to a realistic, subsaturated atmosphere. Since we are in-

terested in idealized waves, a simpler representation of latent heating will be adopted here. To study the effect of convection on frontogenesis, Parker and Thorpe (1995) used a parameterization called ''conditional heating'' in which the latent heat release is proportional to the low-level convergence. We adopt a variant of the conditional heating parameterization in which the static stability is reduced for all ascending parcels, assumed saturated. Since saturation alters the wave at the linear stage (the normal mode itself is different from the dry normal mode), we prefer this parameterization to an explicit treatment of moisture. Conditional heating has been used in numerous theoretical studies (Emanuel et al. 1987; Joly and Thorpe 1989; Montgomery and Farrell 1991; Whitaker and Davis 1994; Fantini 1995). An experiment with explicit moist physics, wherein we initiate the life cycle with a dry normal mode, will be discussed briefly for comparison purposes.

Balasubramanian and Yau (1996, hereafter BY96) found that individual moist and dry life cycles are similar from the point of view of energetics and PV dynamics in Cartesian geometry. We will demonstrate that dry and moist short waves equilibrate similarly to each other on the sphere as well. This allows us to shift our attention from the moist physics, per se, to the issue of zonal scale in trying to understand moist wave equilibration. Thus, much of our discussion here will refer to dry short waves. While the life cycles in Cartesian and spherical geometries exhibit stark differences for long waves (BG97; Whitaker and Snyder 1993), the literature does not indicate whether they are different for short waves. Although the results will not be shown here, we have checked that they are *not* significantly different for short waves. Thus, the ''scale effect'' proposed by Whitaker and Snyder (1993) and the ''barotropic feedback'' invoked by BG97 to differentiate between spherical and Cartesian geometry are no longer applicable. Consequently, we employ spherical geometry for the present experiments.

In summary, our two major objectives are as follows. First, we wish to identify the effect of latent heat release on the life cycles of baroclinic waves on the sphere. Since part of this effect is to shift the wavelength of maximum growth rate to shorter scales, we focus attention on wavenumber 8. This wave and smaller ones are sometimes called ''cyclone'' waves. The suddenness of the transition to cyclone-wave behavior will be clearer if we concentrate on the largest of the short waves. We analyze the differences due to moisture and zonal scale in terms of eddy kinetic energy, surface temperature, and upper-level PV. Second, as a sequel to BG97, we analyze in detail the equilibration of cyclone waves. We try to understand why equatorward momentum fluxes lead to complete barotropic decay in short waves while they lead to long-lived vortices in long waves.

The spherical model and the latent heat parameterization scheme are briefly described in section 2. The results for the short waves are presented in section 3. The equil-

ibration of wavenumbers 5 and 7, a wavenumber 8 experiment with explicit moist physics, and surface drag are discussed in section 4. The proposed classification of equilibration scenarios is detailed in section 5.

2. The model

The spectral model used here and in the wavenumber 6 study of BG97 is described in Held and Suarez (1994) and Bourke (1974). It is a hydrostatic, sigma-coordinate, spectral model. We use 20 equally spaced sigma levels, with the top of the model at zero pressure. A leapfrog scheme is used for time stepping. The horizontal diffusion of vorticity, divergence, and temperature is biharmonic, with the diffusivity chosen to yield an *e*-folding time of 1 h for the shortest wave. To keep the experiments comparable to those of BG97 and THM, we left out surface drag. The truncation is triangular and we impose sector symmetry. For wavenumber 8, we use a resolution of T184. The model output is interpolated to pressure levels for analysis.

a. Parameterization of latent heat release

Here we briefly describe the parameterization of latent heating used in the model. The scheme was developed by Thorpe and Emanuel (1985) to approximate the effect of condensation. All ascending air is assumed saturated and all descending air is assumed dry. For the ascending air, the saturated equivalent potential temperature is conserved, while potential temperature is conserved for the descending parcels. In previous implementations (Emanuel et al. 1987; Joly and Thorpe 1989; Montgomery and Farrell 1991), two-dimensional semigeostrophic models were used and the (slantwise) convective stability was assumed to be either constant or a linear function of height. Fantini (1995) used the parameterization in a three-dimensional, quasigeostrophic model and chose the static stability parameter such that the basic state was exactly neutral to convection. In their Cartesian primitive-equation (PE) model, Whitaker and Davis (1994) allowed the vertical stability in the ascending regions to vary with local temperature and pressure. We follow this last approach for our PE model on the sphere.

For descending air, which is unsaturated, the thermodynamic equation gives

$$\frac{\partial T}{\partial t} = -\mathbf{V}\cdot\nabla T - \omega\frac{T}{\theta}\frac{\partial\theta}{\partial p}, \tag{1}$$

where $\mathbf{V}$ is the horizontal velocity. For the ascending air, Emanuel et al. (1987) show that the temperature is governed by

$$\frac{\partial T}{\partial t} = -\mathbf{V}\cdot\nabla T - \omega\frac{\Gamma_m}{\Gamma_d}\frac{T}{\theta_e}\frac{\partial\theta_e}{\partial p}, \tag{2}$$

where Γ_m and Γ_d are the moist- and dry-adiabatic lapse

rates, respectively, and θ_e is the (saturated) equivalent potential temperature. To change to sigma-pressure coordinates ($\sigma = p/p_s$), we use $\omega(\partial/\partial p) = A(\partial/\partial\sigma)$ where $A = \dot{\sigma} - \sigma(\nabla\cdot\mathbf{V} + \partial\dot{\sigma}/\partial\sigma)$. The quantity A is the same as the vertical pressure velocity, ω, divided by p_s, the surface pressure. Since $\theta_e \approx \theta$ at low temperatures, the effective static stabilities multiplying ω in (1) and (2) are nearly the same in the upper troposphere and polar regions. Since explicit moist convection is not represented, changes in static stability can occur only on synoptic or diffusive time and space scales. Under these conditions, we are obliged to ignore the second term on the right-hand side of (2) if $\partial\theta_e/\partial p > 0$.

b. Initial conditions

The model is initialized with a zonally symmetric jet plus the fastest-growing normal mode at the specified wavenumber. The wave is given an initial amplitude of 1 m s^{-1} for the meridional velocity at the lower boundary. The basic state is shown in Fig. 1a. In the troposphere, the wind and thermal fields are essentially those of BG97 in their simulation of long waves on the sphere. The structure of the jet is given by

$$u = u_0 F(p)\sin^3[\pi(\sin^2\phi)]. \tag{3}$$

The maximum speed of 47 m s^{-1} occurs at $\phi = 45°$ and $p = 175$ mb. The function $F(p)$ is chosen to match the wind field used by THM. The corresponding potential vorticity distribution is shown in BG97. The strength and width of the jet are close to mean winter conditions in the Northern Hemisphere (Holton 1992; Peixoto and Oort 1992). Since we have used 20 equally spaced sigma levels, the tropopause and the stratosphere are not well represented. The barotropic conditions above 175 mb create unrealistic horizontal shear in the stratosphere.

The initial ratio of the moist and dry static stabilities,

$$r \equiv \frac{\Gamma_m}{\Gamma_d}\frac{\theta}{\theta_e}\frac{\partial\theta_e}{\partial\sigma}\bigg/\frac{\partial\theta}{\partial\sigma}, \tag{4}$$

as determined by the initial temperatures, is plotted in Fig. 1b. As mentioned above, negative ratios (initially confined to the Tropics) are replaced by zero for the time integration. The highly nonlinear dependence of saturation equivalent potential temperature on temperature and pressure makes r decrease downward and equatorward. This distribution is similar to that used by Whitaker and Davis (1994).

3. Results

Growth rates as a function of wavenumber are plotted in Fig. 2 for dry and moist waves. These values are obtained by running the full model for long times while renormalizing the perturbation. The curve for the dry waves shows a sharp maximum in growth rate at wavenumber 7, in agreement with Simmons and Hoskins
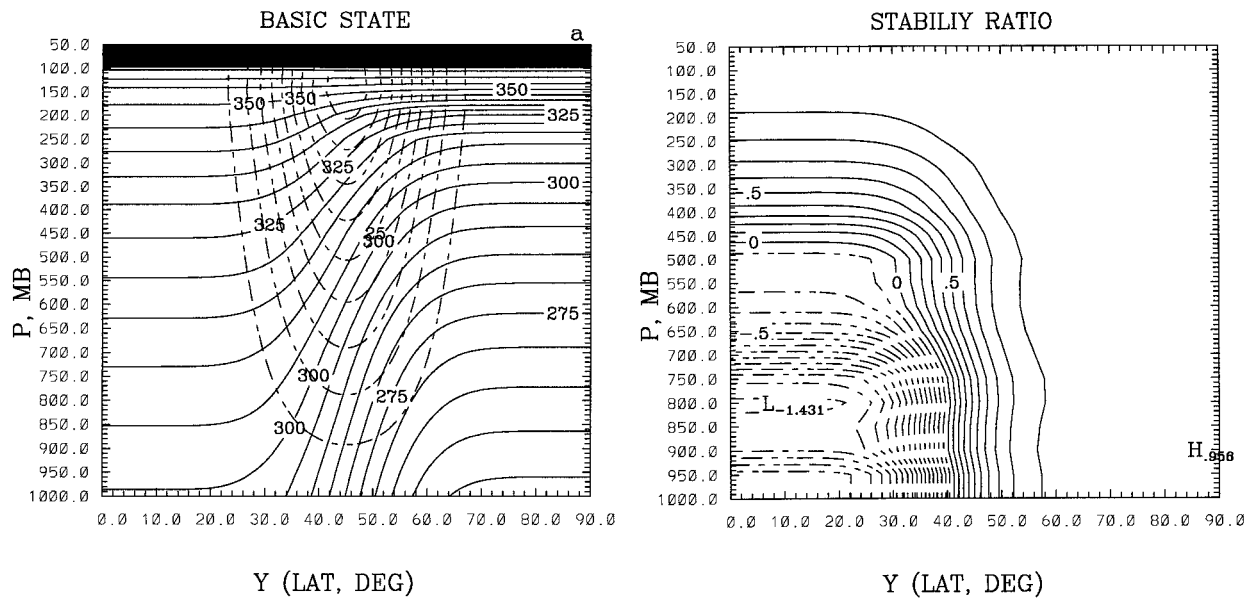
FIG. 1. The initial conditions for the life cycle experiments. (a) Potential temperature (solid lines, every 5 K) and zonal wind (dashed, every 5 m s^{-1}). (b) The ratio of moist to dry static stability, r, as defined in (4). The contour interval is 0.1. The negative values imply conditional instability. Convection is parameterized in these regions by substituting $r = 0$ in the thermodynamic equation for ascent.

(1976). The curve for the moist waves has a flat region of strong instability for wavenumbers 7 and above, as seen before in Emanuel et al. (1987) and Fantini (1995). Thus, the scale selection is substantially removed by latent heating. The instability remains strong at small scales because meridional variations of moist static stability create a meridional "moist PV" gradient even when there is no dry PV gradient (Whitaker and Davis 1994). Since moist wavenumber 12 grows so much faster than its harmonic, wavenumber 6, it was necessary

to remove it explicitly in computing the wavenumber 6 growth rate.

We focus on the moist case of wavenumber 8. Its growth rate is about 1.45 times that of dry wavenumber 6, which was studied in detail in BG97. In their two-dimensional model, Joly and Thorpe (1989) found that in the limit of vanishingly small stability ratio r, the growth rate of the most unstable y-independent moist Eady mode was about 1.9 times that of the corresponding dry mode, with a wavelength 0.6 times as big. It has been noted that wavenumber 6 breaks anticylon-ically to produce anticylonic horizontal shear at low levels. Here we describe the life cycle of a baroclinic wave that breaks cyclonically.
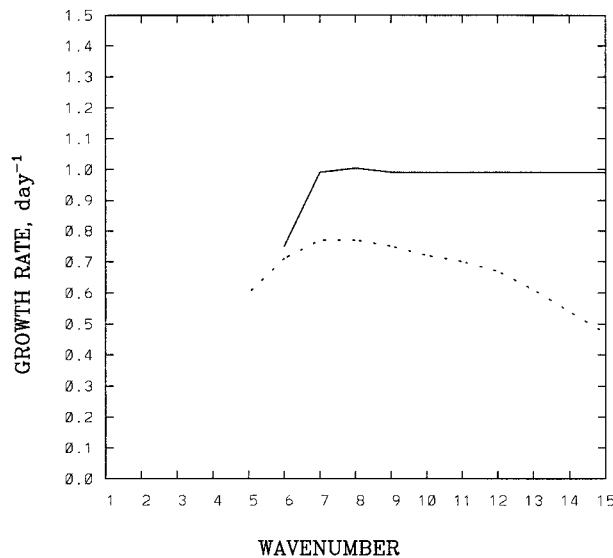
a. Normal modes

The shape of the dry and moist normal modes and their eddy momentum fluxes are shown in Figs. 3 and 4. For clarity, two wavelengths are shown. We will refer to NW–SE orientation as "cyclonic tilt" and NE–SW orientation as "anticyclonic tilt." The modes both have predominantly cyclonic tilt (Fig. 3) and hence equator-ward momentum flux (Fig. 4). This is in sharp contrast to the poleward flux of wavenumber 6 on the sphere (BG97). The tilt of the normal mode depends sensitively on the wavelength, background shear, β effect, and sphericity (Nakamura 1993; BG97) but it is difficult to know, a priori, which effect will dominate.

Since Cartesian normal modes are also tilted cyclon-ically (at all zonal scales), there is a suggestion that the cyclonic tilt of the spherical short wave is made possible by its meridional confinement. In BG97, we argued heu-

FIG. 2. The growth rate curves for dry (dashed) and moist (solid) baroclinic waves on the sphere.
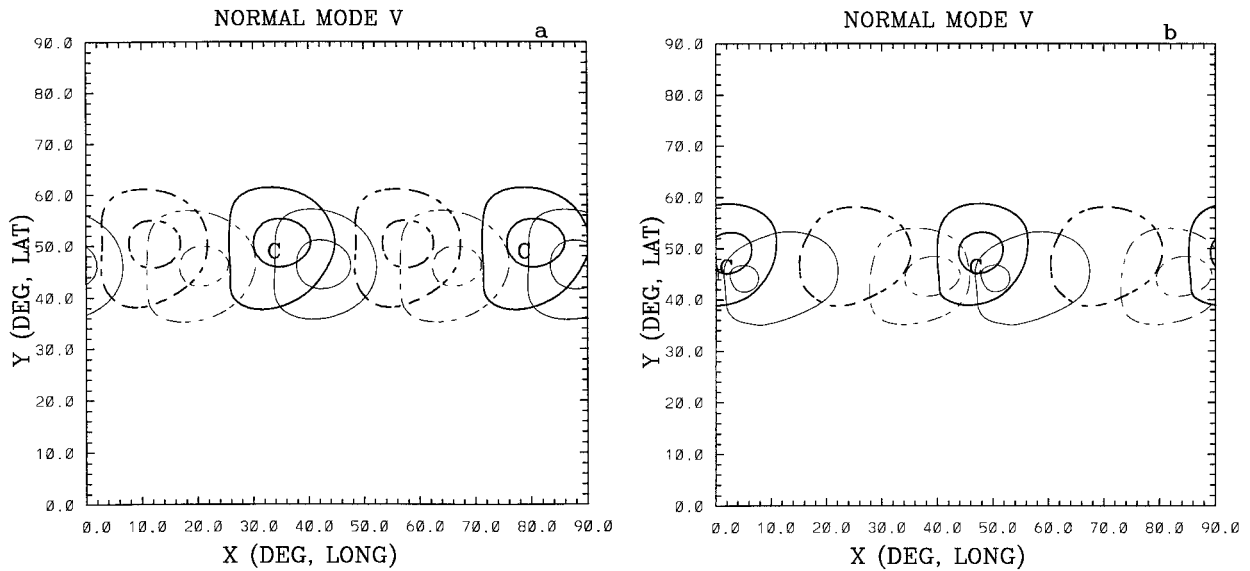
FIG. 3. The wavenumber-8 normal mode meridional velocity at 350 mb (thick lines) and at 1000 mb (thin lines) for the (a) dry and (b) moist baroclinic waves. The contour interval is 0.5 m s^{-1} The fields are normalized at both levels such that the amplitude of the waves is 1.0 m s^{-1}.

ristically that the anticyclonic tilt was due to the latitudinal dependence of the frequency or angular phase speed of edge waves on the sphere. The frequency of barotropic Rossby waves in Cartesian geometry is given by

$$\omega = Uk - \frac{\beta k}{k^2 + l^2}, \qquad (5)$$

where U is the zonal wind speed and (k, l) is the wavenumber vector. The spherical effect may be approxi-

mated locally by letting $k = k_0 \cos\varphi_0/\cos\varphi$ and $\beta = \beta_0 \cos\varphi/\cos\varphi_0$ in (5). Of course, the dependence on latitude, φ, is not permitted in a normal mode. However, when coupled to a "surface PV" type of lower edge wave (e.g., Hoskins et al. 1985), the full eigenmode can compensate by making the *vertical* tilt also vary with latitude. For a growing mode, the temperature anomaly should tilt more downshear with height at higher latitudes and less downshear at lower latitudes. This biases the mode toward anticyclonic *meridional* tilt.
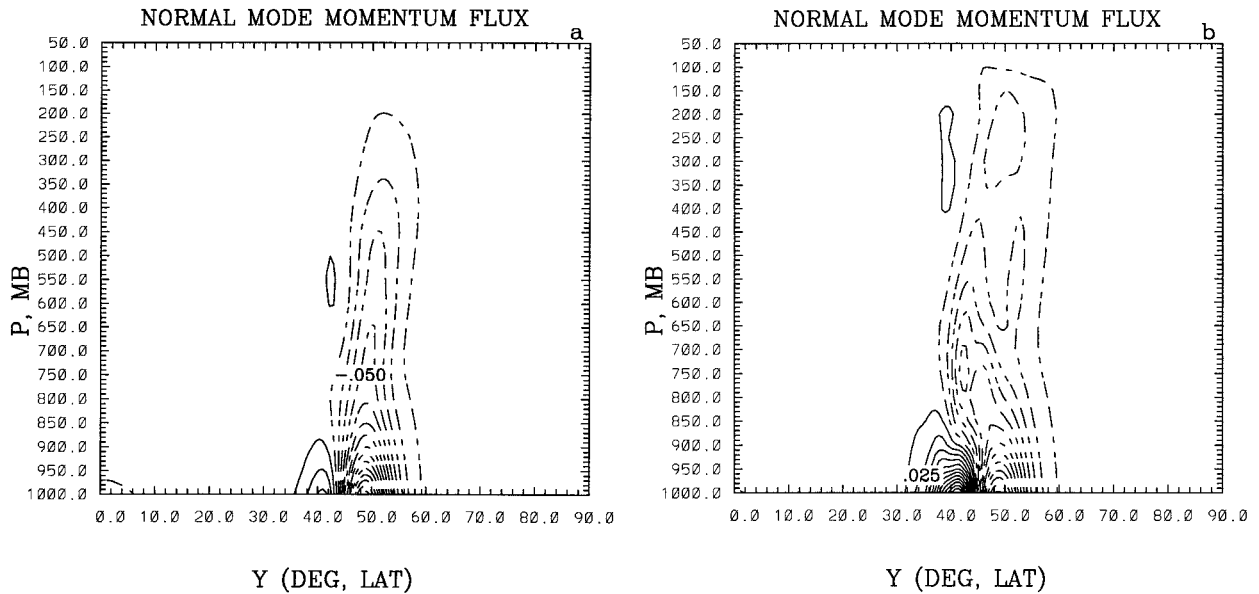

FIG. 4. The wavenumber-8 normal mode zonal-mean eddy momentum flux for (a) dry and (b) moist baroclinic wave. The contour interval is 0.0125 m^2 s^{-2}.
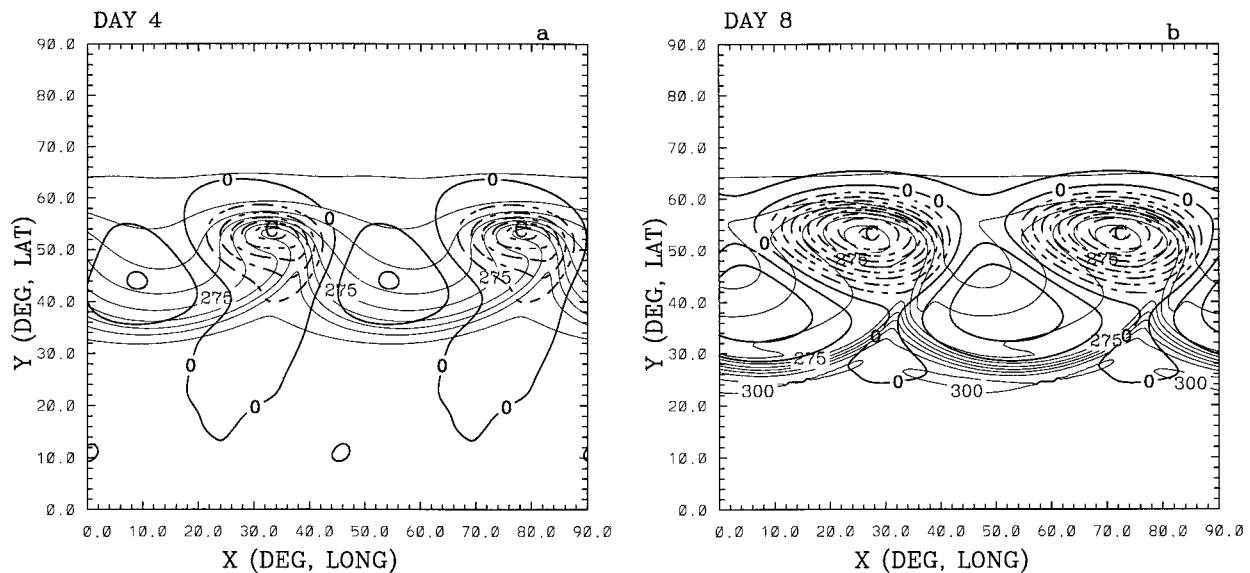
FIG. 5. The geopotential deviation (thick lines, every 5 m² s⁻²) and temperature (thin lines, every 5 K) fields at 1000 mb on (a) day 4 and (b) day 8 for the dry case. The label ''C'' denotes the cyclone center.

Short baroclinic waves are more confined meridionally and are not expected to show as much sensitivity to sphericity. This allows the horizontal shear in the basic state to play a dominant role, as in Cartesian normal modes at all scales. The cyclonic tilt of the Cartesian modes is due to non-quasigeostrophic effects discussed in Snyder et al. (1991) and BG97. The meridional confinement of short waves is apparently due to the narrowing of the zone between upper-boundary critical latitudes as the eastward phase speed increases with wavenumber. In a two-layer QG model, Feldstein and Held (1989) find that the normal-mode amplitude decreases sharply at the linear critical latitudes. We conducted an experiment with a wider jet, obtained by changing the first exponent in (3) from 3 to 1. The normal modes and the zone between critical surfaces at upper levels were both wider by about 10°. The modes acquired considerable anticyclonic tilt and more poleward momentum fluxes, similar to dry wavenumber 6 in the original, narrower jet (BG97).

Moist linear modes have an asymmetry between northerlies and southerlies. In particular, the southerlies are stronger than the northerlies. At low levels, there is a strong zonal gradient of meridonal wind near the trough axis that presages earlier frontal formation. The westward tilt with height is reduced considerably near the cyclone center. These results are in agreement with moist normal modes in a slantwise neutral environment (Emanuel et al. 1987).

b. Synoptic evolution

In Figs. 5 and 6, we have plotted the fields of 1000-mb temperature and geopotential deviation from the initial basic state for the dry and moist waves on day 4 and day 8. The poleward migration of cyclones and equatorward migration of anticyclones, typical of baroclinic wave development, can be seen in both the dry and moist cases on day 4. In both cases, the cyclones exhibit the horizontal tilt associated with equatorward momentum fluxes. However, latent heat release has altered the moist solution significantly by selectively intensifying the cyclones. The anticyclone intensity is similar to the dry case. The warm core ''seclusion'' (closed low-level temperature contours) and bent-back warm front in Fig. 6a are well-known features of moist cyclogenesis (Shapiro and Keyser 1990; Hedley and Yau 1991; Balasubramanian and Yau 1994b). These features are related to the process of warm-air ''seclusion,'' which we will discuss below in regard to long-term equilibrated states.

By day 8, the cyclones have migrated to 54° and 52° lat in the dry and moist cases, respectively. This is quite different from the anticyclonic wavenumber 6 life cycle discussed in BG97, in which the cyclones had moved to 65° by the same time. The difference is due to the poleward momentum fluxes in the long wave and equatorward fluxes in the short wave. Compared to wavenumber 6, the present eddies remain confined meridionally. The closed temperature contours encompass a much smaller region than in the cyclonic long-wave life cycle, in which the cyclones become axisymmetric and remarkably persistent (THM). In the short wave, the vortices continue to transfer energy to the zonal-mean wind, as indicated by the elongation of the temperature and geopotential contours on day 8.

The cyclone and frontal zones in the moist solution have attained much greater intensity than those in the dry solution on day 8, but the wave tilt and type of equilibration are similar. This result is in agreement with
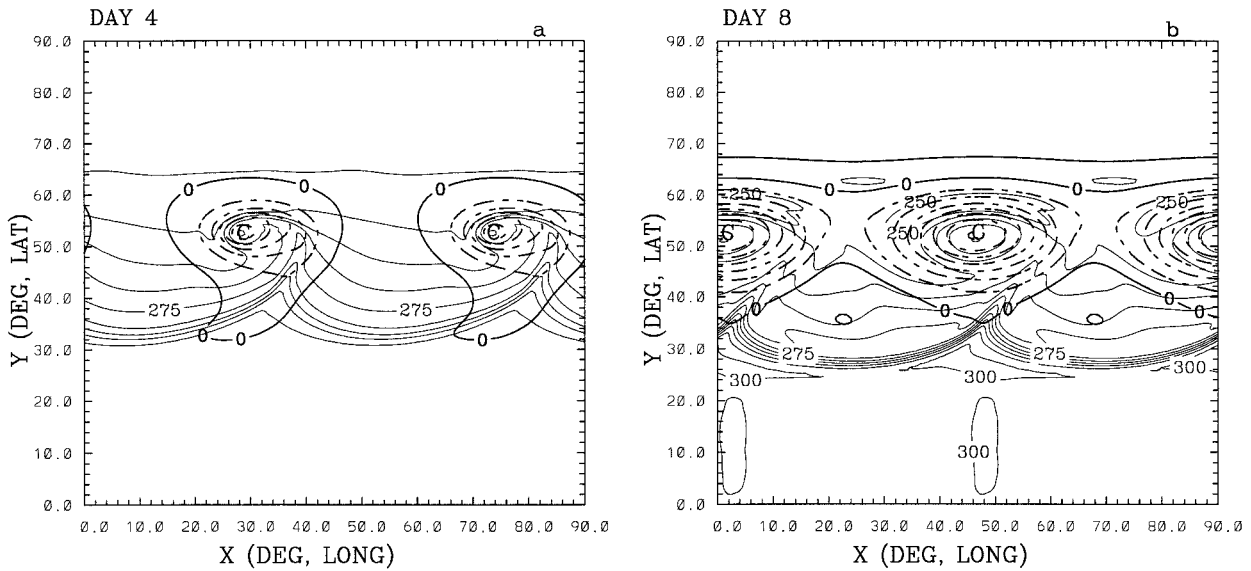
FIG. 6. Same as in Fig. 5 but for the moist case. The contour intervals for geopotential in (a) and (b) are 10 m² s⁻² and 15 m² s⁻², respectively.

BY96, in which it was shown that the moist and dry cyclones are broadly similar from the point of view of energetics and "PV thinking" as well.

In Figs. 7 and 8, we have plotted the PV field on the $\theta = 330$ K surface for the dry and moist waves, respectively, for days 4 and 8. The $\theta = 330$ K surface is located at 350 mb in the tropical regions and passes through the tropopause in midlatitudes. The cyclonic tilt of the contours in the dry wave is clear on day 4 (Fig. 7a). The moist solution at this time (Fig. 8a) is near its maximum in total eddy energy and bears some resem-

blance to the fully equilibrated cyclonic long-wave life cycle (THM's LC2) and the Cartesian long-wave life cycle (BG97). The resemblance is due to the cyclonic tilt of the eddy and, in the moist solution, the vertical alignment of the low centers. The vertical alignment of the low pressure in the moist solution, as indicated by the locations of the surface and upper-level cyclonic vortices, is due partly to the shrinking of horizontal scales by the influence of moisture and partly to a zonal phase alignment.
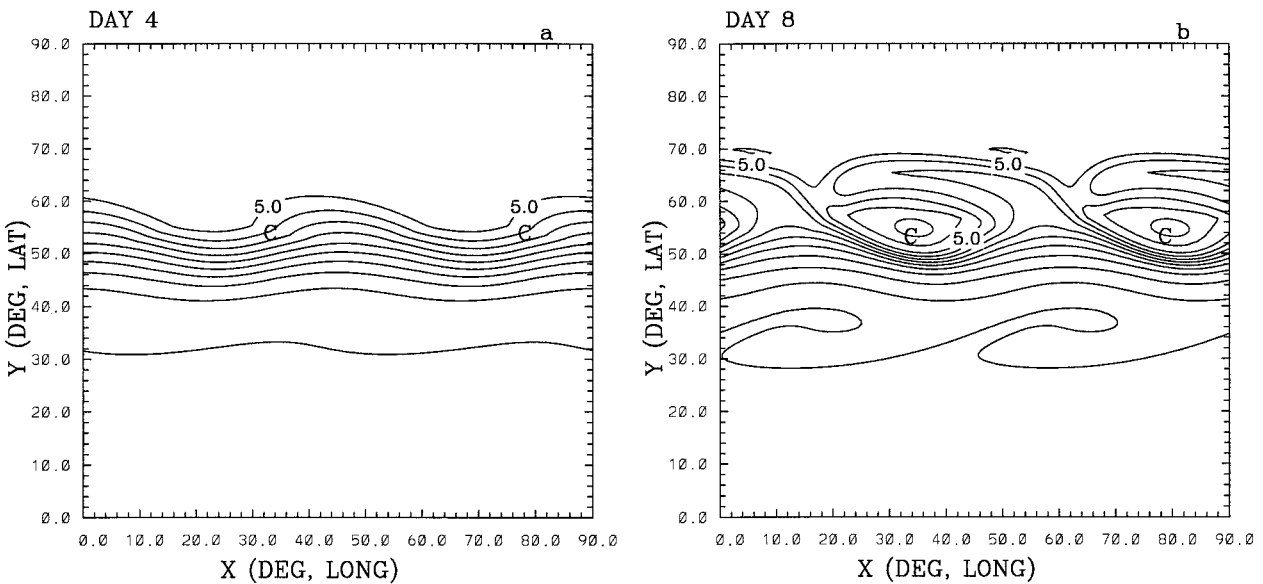
On day 8, zonally elongated cyclonic vortices have

FIG. 7. The potential vorticity field on $\theta = 330$ K surface on (a) day 4 and (b) day 8 for dry wavenumber-8 life cycle. The contour interval is 0.5 pvu. The label "C" denotes the surface cyclone center.
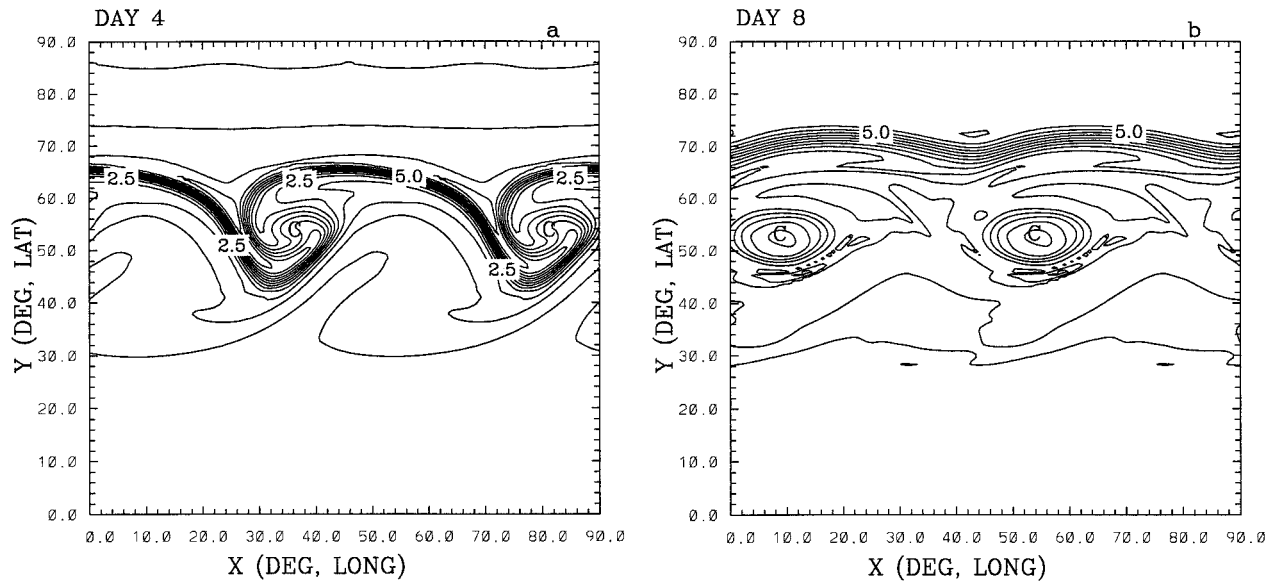
FIG. 8. Same as in Fig. 6 but for the moist wave.

formed in the dry case (Fig. 7b) and smaller cutoff cyclones have appeared in the moist case (Fig. 8b). Like the closed surface temperature contours, these vortices are much smaller in proportion to wavelength than in cyclonic wavenumber 6. The zonally averaged PV (not shown) is well mixed in a roughly 25° band that encompasses the cutoff vortices. This is narrower than in the long-wave life cycle, where the mixed zone stretches across 35 degrees of latitude. The crowding of PV contours around 70° in the moist short-wave solution is associated with intense easterlies, as we will see in section 3d.

The dry wave has still not fully equilibrated at the time

of Fig. 7b. Open contours retain cyclonic tilt and the isolated vortices continue to elongate. In general, small-scale structures are more vulnerable to diffusion. In a balanced flow, the depth of influence of surface temperature and PV features is proportional to their horizonal scale. As a result, the short-wave vortices are also more vulnerable to deformation by larger-scale structures.

c. Energetics

In Fig. 9a, we have plotted the geopotential perturbation at the cyclone center as a function of time. The
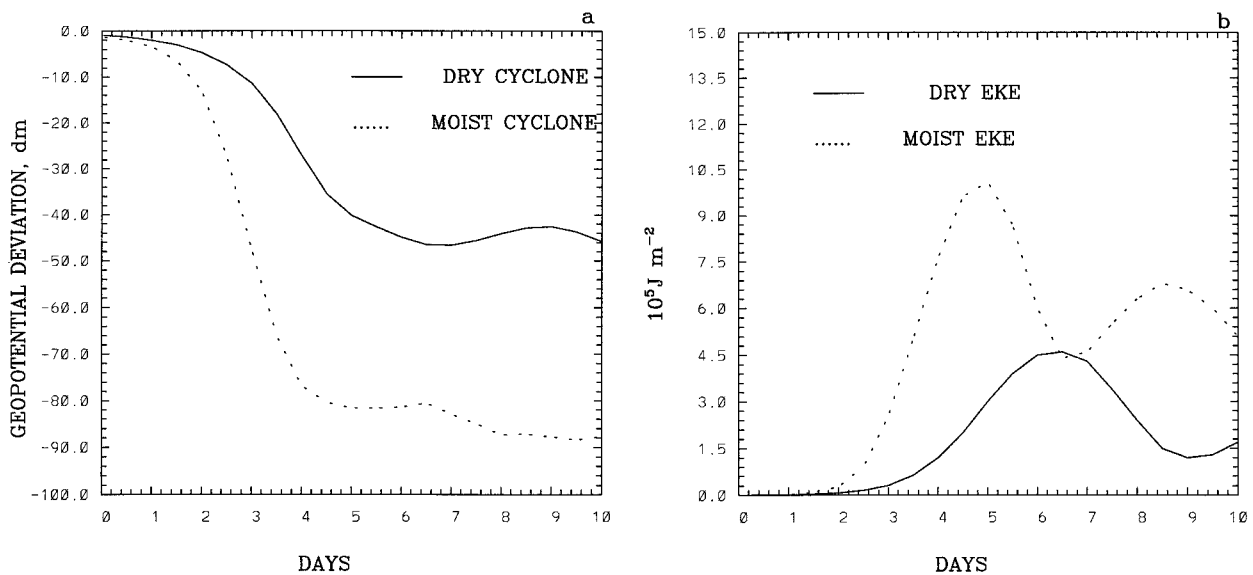
FIG. 9. The evolution of (a) geopotential deviation at the surface cyclone center and (b) the domain-averaged eddy kinetic energy for the dry (solid) and moist (dashed) wavenumber 8 life cycles.
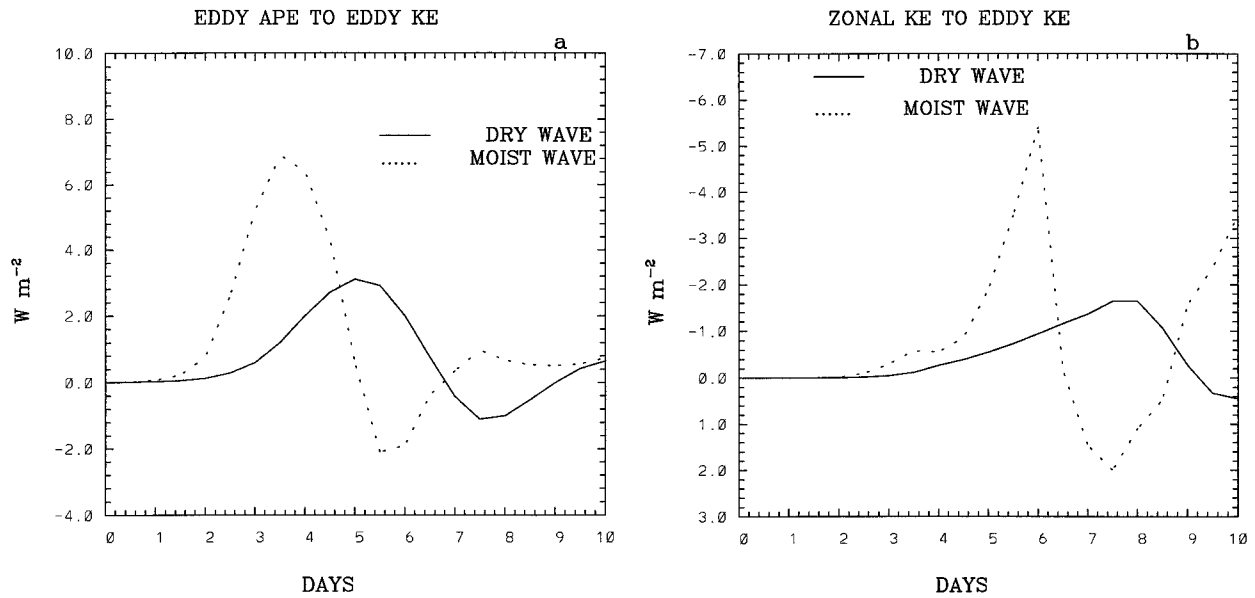
FIG. 10. The evolution of domain-averaged (a) baroclinic conversion (eddy APE to eddy KE) and (b) barotropic decay (zonal KE to eddy KE) for the dry (solid) and moist (dashed) wavenumber-8 life cycles.

moist cyclone undergoes a sharp 48-h deepening of about 65 dm between days 2 and 4. The eddy kinetic energy (EKE) evolution (Fig. 9b) also indicates a steep increase during this period. The dry cyclone deepens more gently and to only half the maximum intensity of the moist cyclone, as measured by both minimum geopotential anomaly and maximum EKE. The moist cyclone reaches its maximum EKE on day 5 while the dry cyclone does so after 1.5 more days. There is a secondary peak in EKE on day 8.5 in the moist case.

The time series of energy conversion from eddy APE (available potential energy) to EKE is shown in Fig. 10a. The definitions of EKE and APE and expressions for baroclinic conversion and barotropic decay are given in BG97. The maximum baroclinic conversion rate in the moist case is twice that in the dry case. After day 4, baroclinic conversion declines sharply in the moist case, with a brief period of baroclinic decay between days 5 and 7. The baroclinic conversion is qualitatively the same in the dry wave, which exhibits baroclinic decay between days 7 and 9. The baroclinic decay is associated with sinking motion over the occluded cyclone, as we show in section 3e. For the moist wave, there is a secondary maximum in baroclinic conversion at day 7.5.

Significant conversion of EKE to ZKE (Fig. 10b) begins on day 4 in the moist wave and lasts only 2 days. The peak on day 6 corresponds with the sharp decline in EKE (Fig. 9b) in the moist wave. The peak in barotropic conversion is as sharp as in the dry wavenumber 6 discussed in BG97, but the present wave exhibits stronger baroclinic conversion than the long wave during its relatively brief growth phase. The barotropic decay reverses its sign between days 6.5 and 8.5 in the moist wave, indicating that eddies are gaining energy from the zonal-mean flow. This

reversal is associated with poleward, or upshear, momentum fluxes (not shown) on the cyclonic side of the narrow surface easterly zone. The episode of barotropic growth coincides with the aforementioned secondary peak in baroclinic conversion and leads up to the second peak in EKE (Fig. 9b). The possible role of barotropic instability in the reversal of kinetic energy conversion is discussed in section 3d.

d. Development of the zonal-mean wind

In BG97, we found that the low-level momentum flux convergence cooperated with the forcing by the mean meridional circulation to a greater degree in the anticyclonic long-wave life cyle on the sphere (LC1) than in the cyclonic life cycle. Not only were the two sources of zonal-mean momentum more nearly in phase but also the flux convergence was displaced to the poleward side of the westerlies in LC1. This progressively shifted the low-level jet (LLJ) poleward and expanded the shear zone. In the cyclonic life cyle on the sphere and in Cartesian geometry, the meridional circulation opposed any equatorward migration of the LLJ. The barotropic decay was weaker in that case, and large, coherent cyclones were able to develop. Although momentum fluxes are equatorward for short waves, we saw in section 3c that the waves nevertheless experience complete barotropic decay. This prompts us to look closely at the LLJ during the short-wave life cycle.

We will describe the LLJ behavior for the dry wave only. The moist wave equilibration is similar. The mean zonal wind acceleration on the sphere is determined by

EDDY ANGULAR MOMENTUM
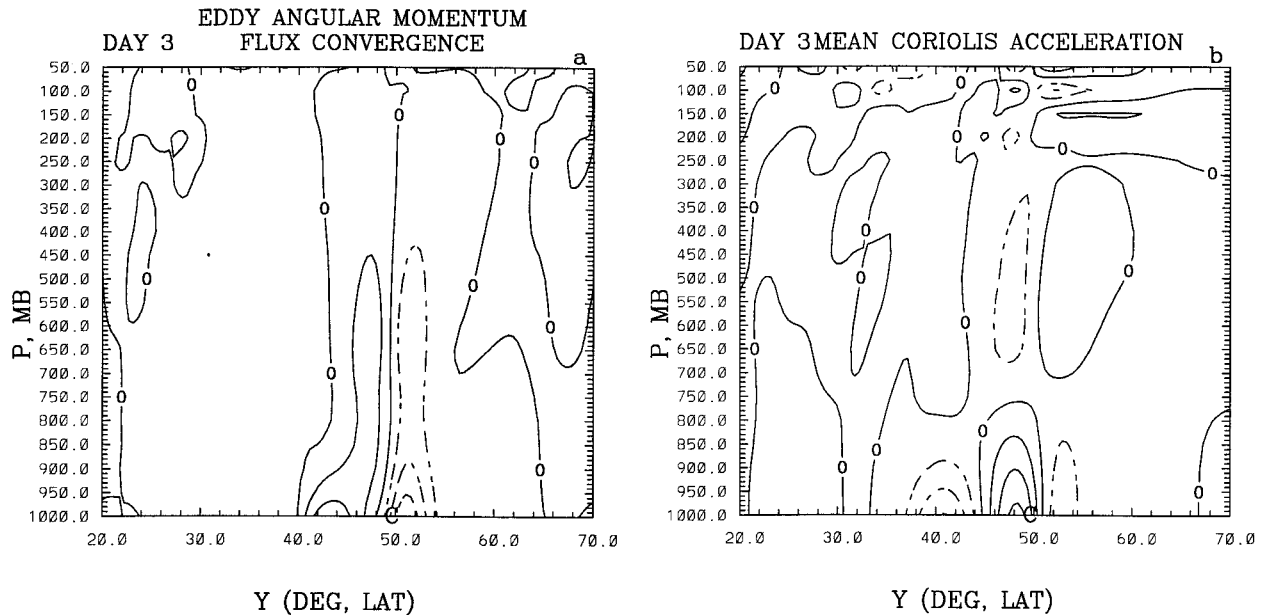DAY 3 FLUX CONVERGENCE

DAY 3 MEAN CORIOLIS ACCELERATION

FIG. 11. (a) The convergence of zonally averaged eddy angular momentum flux and (b) the mean Coriolis acceleration for the dry wavenumber 8 on day 4. The contour interval is 1.0×10^{-5} m s^{-2}. The solid lines indicate westerly acceleration and dashed lines indicate easterly acceleration.

$$\frac{\partial [u]}{\partial t} = -\frac{\partial ([u'v'] \cos^2 \phi)}{a \cos^2 \phi \partial \phi} - \left(\frac{\partial ([u] \cos \phi)}{a \cos \phi \partial \phi} - f \right) [v]$$

$$- [\omega][u]_p - [\omega'u']_p, \qquad (6)$$

where $[\cdot]$ represents zonal average. The first term, representing angular momentum flux convergence, may be expanded as

DAY 6 EDDY MOMENTUM FLUX

FIG. 12. Meridional cross section of zonally averaged eddy momentum fluxes on day 6 for the dry wavenumber-8 life cycle. The contour interval is 5 m^2 s^{-2}.

$$C = -\frac{\partial [u'v']}{a \partial \phi} + \frac{2[u'v'] \tan \phi}{a}. \qquad (7)$$

The first part of (7), representing the ordinary momentum flux convergence, and the Coriolis term, $f[v]$, in (6) are mainly responsible for the acceleration.

The angular momentum flux convergence, C, and Coriolis term, $f[v]$, for day 3 are plotted in Fig. 11. Since the momentum fluxes are almost entirely equatorward, a dipole pattern of westerly (equatorward of 50°) and easterly (poleward of 50°) acceleration is seen (Fig. 11a). The tendency is mainly barotropic. The mean Coriolis acceleration has baroclinic structure (Fig. 11b) and is eroding the baroclinicity in the jet while increasing it at higher and lower latitudes. The two sources of low-level momentum are not well correlated during the linear development, unlike the rapidly zonalizing long-wave life cycle. Since barotropic decay continues well past the low-level saturation time, the flux convergence will eventually dominate the Coriolis acceleration. However, their cooperation in the early stages is important because the momentum fluxes feed back on the zonal-mean wind to amplify the effect of the forcing. In BG97, we argued that this particular feedback, the so-called "barotropic governor" (James 1987; Nakamura 1993), had to be weakened—for example, with additional cyclonic barotropic shear (THM)—in order to avoid rapid barotropic decay. For reasons discussed in the next subsection, even the weakened feedback is not too weak to destroy the wave at this scale.

The meridional cross section of zonally averaged eddy-momentum fluxes on day 6 is plotted in Fig. 12.
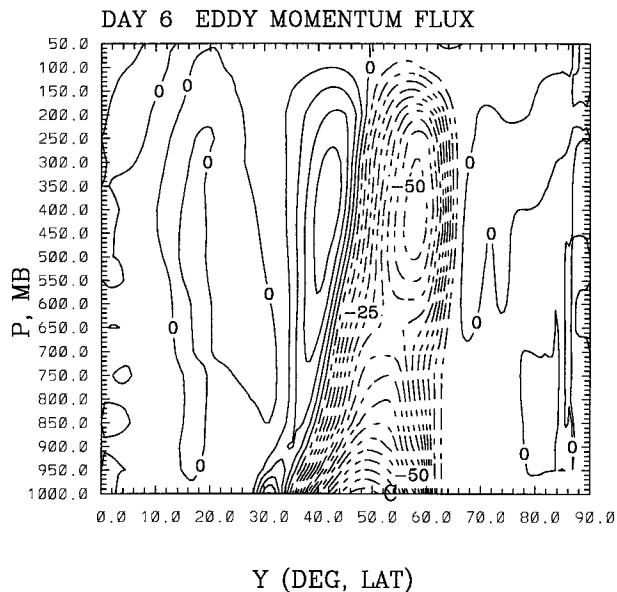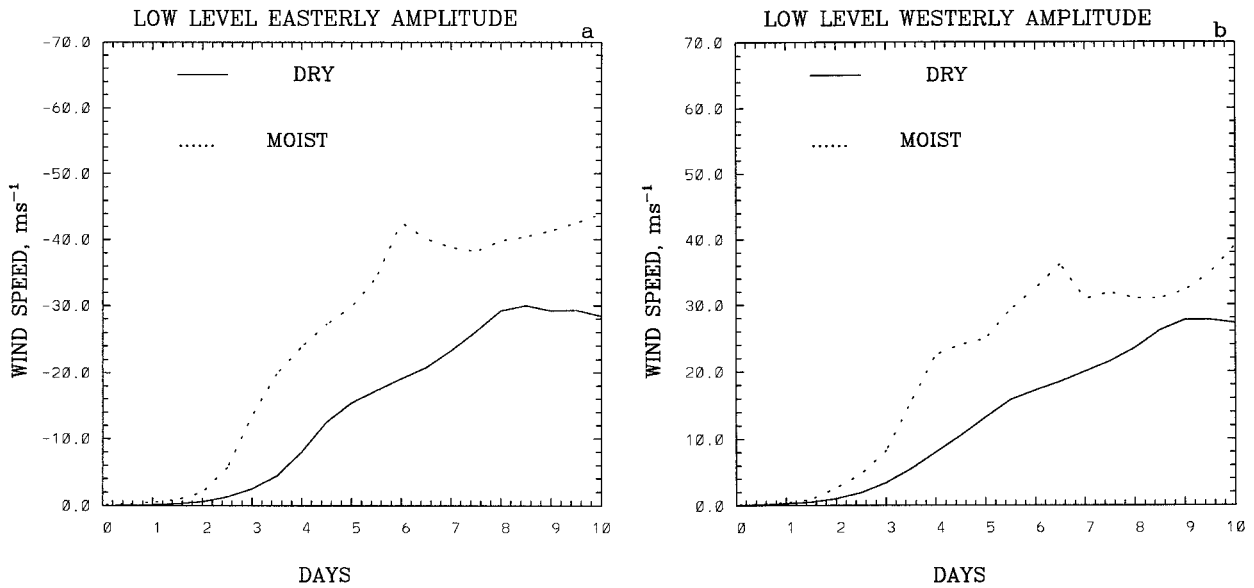
FIG. 13. The evolution of maximum low-level (a) easterly and (b) westerly wind speed in dry (solid) and moist (dashed) wavenumber-8 life cycles.

This time is well into the decay phase. Equatorward momentum fluxes now extend to all levels of the troposphere. The forcing of easterlies between 50° and 60° is evident. The equatorward fluxes have doubled in amplitude since the wave saturated on day 4.5, indicating the feedback in the barotropic decay process. The equatorward fluxes have broadened since the saturation, but are still much narrower than the poleward fluxes in wavenumber 6 (BG97).

In Fig. 13, we have plotted the maximum low-level (1000 mb) easterly and westerly wind speeds as a function of time. The lack of surface drag makes the winds unrealistically strong at this level. The distance between the barotropic jets is about 1000 km. The amplitude of the mean easterly wind reaches 30 m s^{-1} on day 8 in the dry wave and 43 m s^{-1} on day 6 in the moist wave. The low-level westerlies are not as strong (Fig. 13b). For wavenumber 6 baroclinic life cycles, the westerly amplitude at the surface was greater than the easterly amplitude (BG97). For wavenumber 8, the easterly acceleration is comparable to the westerly acceleration on day 4 and becomes larger later on. The lateral wind shear is of the order of 50 m s^{-1} per 1000 km on day 8. In the moist solution, we believe that the zonal-mean flow becomes barotropically unstable between days 6.5 and 8.5. The corresponding reversal in sign of barotropic decay was seen previously in Fig. 10b. Barotropic instability of zonal-mean flow was also observed in the anticyclonic equilibration of wavenumber 6 in BG97.

The deviation of zonal-mean winds from the basic state for the dry wave on day 4, shown in Fig. 14a, consists of westerlies centered at about 50° and easterlies at 56° and 36° at lower levels. The high-latitude easterlies are associated with the cyclones and the low-

latitude easterlies with the anticyclones. In both the dry and moist waves, the maximum easterly wind moves from 55° to 60° during the life cycle, while the westerly jet moves from 45° to 50°. The nearly barotropic nature of the zonal wind deviation on day 8 (Fig. 14b) resembles LC1, but the shear is cyclonic.

e. Baroclinic decay and warm core seclusion

The baroclinic decay in the domain-averaged energy budget is associated with certain lower-tropospheric developments that are more prominent in the cyclonic life cycles (wavenumber 8 and LC2) than in anticyclonic life cycles (LC1). As mentioned in section 3b, the cyclonic life cycles produce a core of warm air at the lower boundary and this feature eventually drifts beneath upper-level cold advection. The quasigeostrophic response is subsidence over the surface low center, with negative baroclinic conversion. "Seclusion" of warm air has been described from observations (Shapiro and Keyser 1990; Neiman and Shapiro 1993a,b) and numerical simulations (Kuo et al. 1991; Hedley and Yau 1991). Balsubramanian and Yau (1994a) showed that it was strongest in moist cyclones. We saw in section 3b that the size of the warm core and the meridional extent of the (zonal mean) PV mixing are highly dependent on wavenumber. We now examine the seclusion process in greater detail as a possible reason for the different types of cyclonic equilibration.

In Fig. 15, we have plotted the departure of 1000-mb temperature from the zonal mean along with the low-level (975 mb) vertical pressure velocity on day 5 and day 7.5. Two centers of warm air, one associated with the seclusion near the cyclone center and the other with
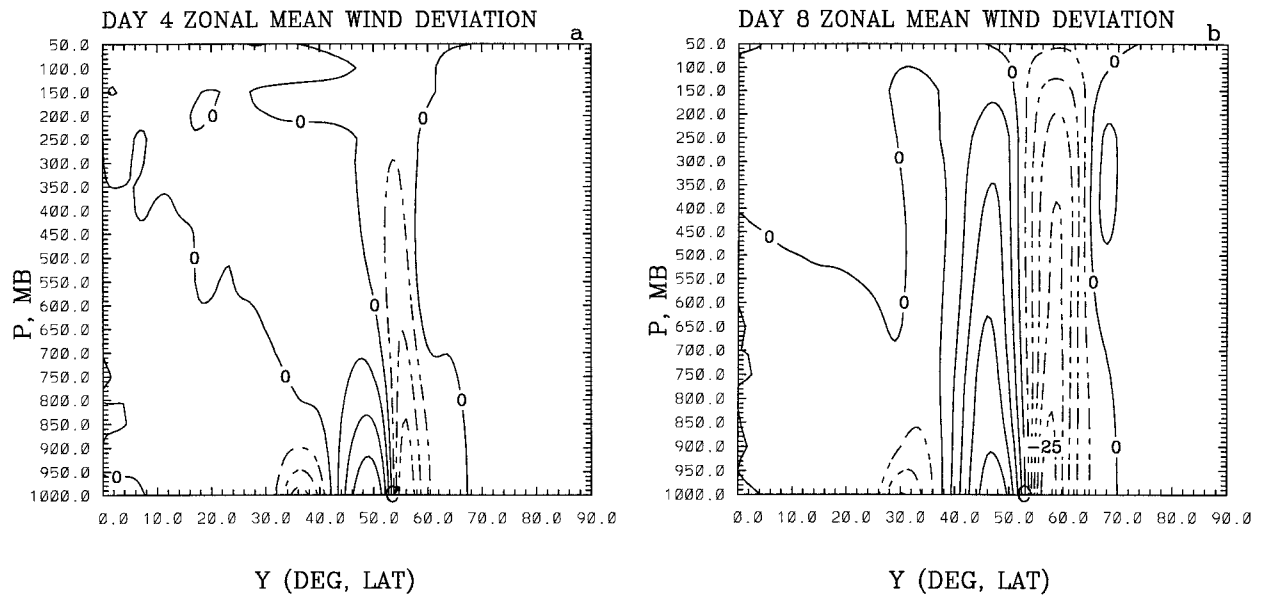
FIG. 14. The zonal-mean wind deviation from the basic state on (a) day 4 and (b) day 8 for the dry wavenumber-8 life cycle. The contour interval is 5 m s^{-1}.

the "warm sector," can be noted. Although the vertical velocity has started developing finer scales by day 5, there is, in general, ascent of the warm air and descent of the cold air at this time, corresponding to baroclinic growth. However, on day 7.5, the warm air surrounding the cyclone center is sinking and the cold air is rising to the east, converting EKE back to eddy APE. Consistent with this baroclinic decay, we notice zonal-mean southward heat transport on day 7.5 (not shown).

The anticyclonic long-wave life cycle (LC1) does not exhibit the same degree of cyclonic wrapping of frontal regions and bent-back warm front formation (BG97). Instead, the temperature contours are strongly sheared out by the anticyclonic barotropic shear so that the surface warm anomaly moves to the northeast of the cyclone. To the west of the cyclone, the gradients are weaker in the anticyclonic life cycle and there is no significant seclusion of warm air. Accordingly, baro-
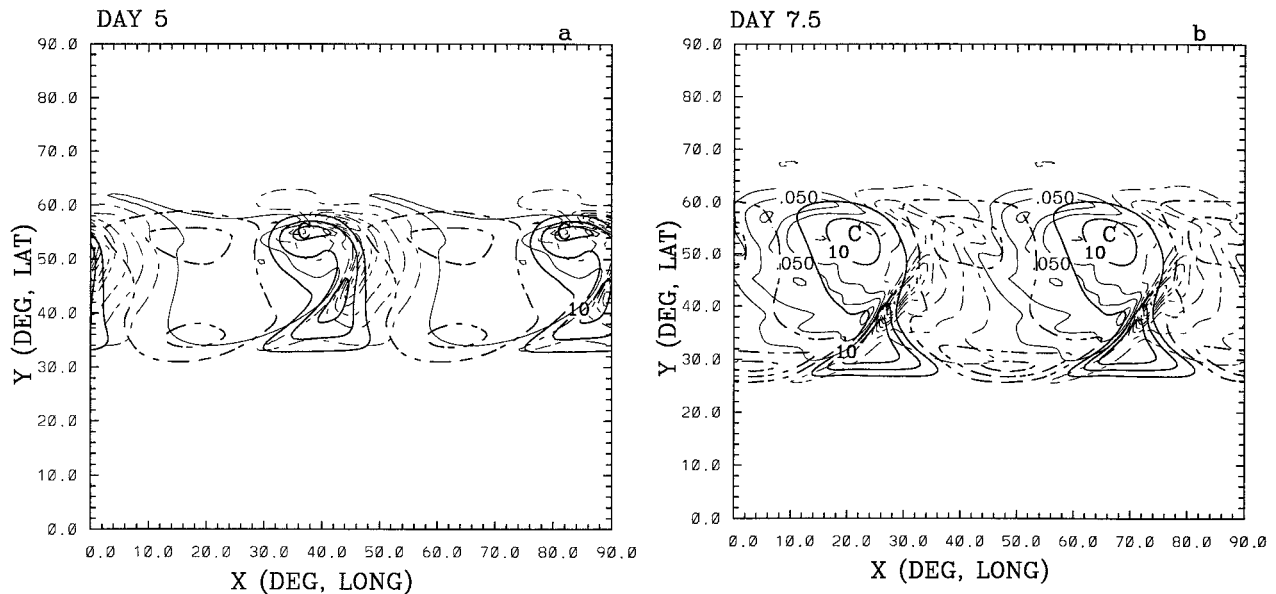

FIG. 15. The zonal-mean temperature perturbation at 1000 mb (thick lines, every 5 K) and the pressure velocity at 975 mb (thin lines, every 0.030 Pa s^{-1}) on (a) day 5 and (b) day 7.5 for the dry wavenumber-8 life cycle. Positive (negative) values of pressure velocity correspond to sinking (rising) motion. The label "C" denotes the surface cyclone center.

clinic decay was not observed in the standard wavenumber 6 life cycle.

Warm-air seclusion is part of the cyclonic wave saturation process in both long and short waves, but the amount of warm air isolated in this process is smaller in short waves than in long waves. Since the latitudinal scale of a wave places a bound on the meridional temperature and PV exchange, the most obvious reason for the difference is the meridional confinement at the higher wavenumbers. Figure 16 compares the evolution of surface θ for wavenumber 8 and cyclonic wavenumber 6. The warm front in the latter (LC2) is much more intense (Figs. 16a and 16d), while the cold front is much stronger in wavenumber 8. On account of its slightly greater linear growth rate, the temperature wave is better developed in wavenumber 8 (Fig. 16a) on day 4 and the tongue of warm air near the cyclone center is narrower. Wave saturation and warm air seclusion take place in wavenumber 8 around day 4.5. During the next two days, there is considerable wrapping of the warm temperature filament around the warm core.

Horizontal divergence helps keep the cold air at lower latitudes from ''rolling up'' into cold cores. The spreading of cold air is directly associated with filamentation of the warm tongues during and following the low-level saturation. From day 5, when baroclinic conversion peaks (Fig. 10a), surface isotherms can be seen cutting off to form the warm core. The first contour to cut off is 286 K around day 5. The 280-K contour cuts off by day 6 (Fig. 16b) and the 275-K contour by day 6.5. In the cyclonic long wave (Fig. 16e), warm core seclusion takes place on day 6 and the first isotherm to cut off is 290K, 4K warmer than in wavenumber 8. The delay in seclusion allows more warm air to be advected into the cyclone center and the warm anomaly to grow larger (Fig. 16f). Note that the 275-K isotherm in wavenumber 8, after shedding its filament, is zonally elongated by the geostrophic deformation (Fig. 16c), whereas the initially kidney-shaped cutoff isotherms in the long-wave solution continue to shed filaments and grow more circular.

The role of low-level cold advection in the timing of the warm core seclusion is illustrated in Fig. 17. We have plotted the 1000-mb warm tongue temperature at 45° lat as a function of time for wavenumber 8 and cyclonic wavenumber 6. The temperature increases due to meridional advection for the first 4.5 days in wavenumber 8. From day 4.5 onward, a sharp decrease in temperature is associated warm core seclusion. The cooling in the warm tongue at this level is due to horizontal diffusion, as there is no significant upward or equatorward advection. In the long wave, the warm advection continues until day 8. In BG97, we showed that the baroclinic conversion peaked on day 7 for this wavenumber, consistent with the delayed saturation and seclusion.

Some characteristics of low-level saturation in ''cyclonic'' baroclinic waves are listed in Table 1. The area inside the cutoff 280-K contour, which roughly measures the amount of secluded warm air, increases as the wavenumber decreases. The area is an indicator of the size of cyclonic vortex. The meridional size of the vortex is limited by the maximum meridional displacement of the isotherms on the 1000-mb surface. The inference from Table 1 is that a relatively large amount of warm air is secluded in LC2. Thus, a significant difference between LC2 and wavenumber-8 exists in the size of cyclonic vortices.

f. EP cross sections

The principle of wave activity conservation has provided succinct descriptions of baroclinic life cycles as well as extratropical general circulation dynamics (e.g., Edmon et al. 1980; Held and Hoskins 1985; THM). At small amplitude, wave activity propagates with the Eliassen–Palm (EP) flux vector, which is defined in terms of the rectified eddy momentum and heat fluxes. According to the classical view, the linear growth stage is dominated by vertical propagation and an EP flux divergence that accelerates the flow at lower levels and decelerates it at upper levels. During the barotropic decay stage, when the momentum flux divergence dominates, there is horizontal propagation of wave activity into the subtropics. The mean flow is decelerated there and accelerated in middle latitudes. While the midlatitude upper-level flow is more or less unmodified at the end of a life cycle, irreversible mixing has accelerated the mean flow in the midlatitude lower troposphere and decelerated it in the subtropical upper troposphere.

This picture has been confirmed for transient eddies in observations (Edmon et al. 1980; Randel and Held 1991) and for a single cyclogenesis event in the Southern Hemisphere (Randel and Stanford 1985). In short waves, since the eddy momentum fluxes remain equatorward during the entire life cycle, it is clear that the irreversible upper-level modification should occur on the poleward side of the jet rather than in the subtropics in that case. For the short-wave life cycle, we have computed the EP flux,

$$\mathbf{F} = (F_\varphi, F_p)$$

$$= \frac{2\pi a^2 (\cos\varphi)^2}{g} \left(-[u'v'], \frac{af[v'\theta']}{[\theta]_p} \right), \qquad (8)$$

and its divergence $\boldsymbol{\nabla}\cdot\mathbf{F} = \partial F_\varphi/\partial\varphi + \partial F_p/\partial p$, where a is the radius of earth and the other symbols have their usual meanings (Edmon et al. 1980). When EP fluxes are divergent, the zonal-mean flow is accelerated locally and eddy activity propagates away from that region, and vice versa.

The EP diagrams for the dry wavenumber 8 on days 3, 5, and 7 are in Fig. 18. On day 3 (Fig. 18a), the diagram resembles the normal-mode picture for Charney modes (Edmon et al. 1980). The fluxes are convergent in the lower troposphere where the eddy activity is increasing. They are divergent at the lower boundary where the zonal winds are accelerated. At this time, the EP vectors point
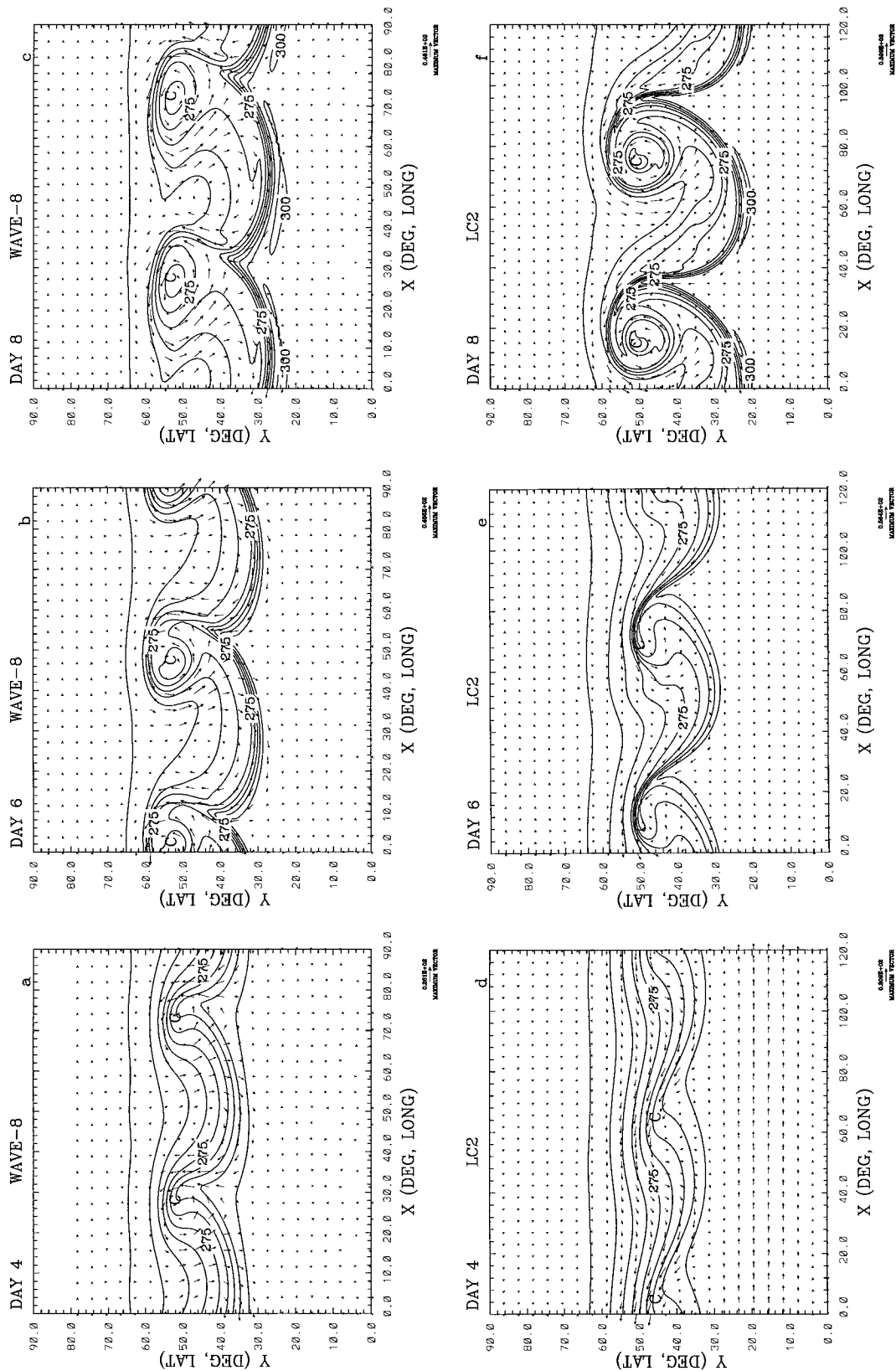
FIG. 16. The temperature and wind fields at 1000 mb on days 5, 6, and 7 for wavenumber 8 (a, b, c) and cyclonic wavenumber 6 (d, e, f). The latter is essentially the same as "LC2" in Thorncroft et al. (1993). The contour interval is 5 K.
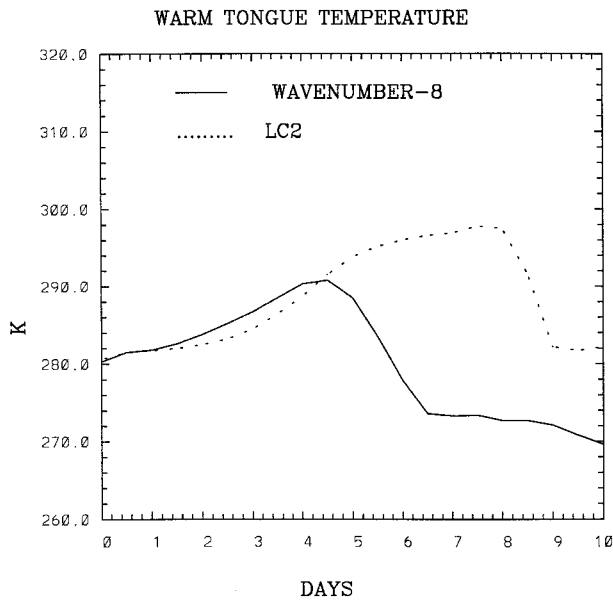
WARM TONGUE TEMPERATURE

FIG. 17. The evolution of maximum temperature in the warm tongue region at 45° for wavenumber 8 (solid) and our simulation of LC2 (dashed).

almost vertically since there is strong baroclinic growth and weak barotropic decay. The arrows also point horizontally with a slight bias toward the pole, in association with equatorward momentum fluxes.

By day 5 (Fig. 18b), the appearance of divergence at the ground implies transfer of wave activity to other latitudes and heights. Note that much of this activity remains at low levels, as indicated by the low-level convergence at 32° and 55°. The other convergence center has shifted upward and slightly poleward. The EP vectors poleward of 40° suggest some propagation toward the equator as well. At this stage, the baroclinic conversion (Fig. 10a) is at its peak and barotropic decay begins to rise sharply (Fig. 10b). Between day 6 and day 8, the wave saturates, starting at low levels. On day 7 (Fig. 18c), the main divergent region has moved upward, signifying zonal wind acceleration over a deeper layer. The EP vectors are mostly horizontal, indicating weak heat fluxes but continuing barotropic decay of the saturated wave. In the lower troposphere, the vectors point slightly downward, signifying baroclinic decay (cf. Fig. 10a).

This picture differs from that for wavenumber 6 of

Simmons and Hoskins (1978) (Edmon et al. 1980; THM) in that the breaking is cyclonic and the main upper jet deceleration occurs poleward of the jet axis. In their analysis of 11-yr and 5-yr averaged data, Edmon et al. (1980) noticed a strong convergent region at 50° and 400 mb in the EP diagrams for transient eddies. They suggested that the reasons for its absence in the wavenumber 6 life cycle could be the model's suppression of baroclinic instability at high latitudes and the restriction to zonal wavenumber 6 and its harmonics. A convergent region on the poleward side of the jet has also been observed in GCMs (Lee and Feldstein 1996). Our results suggest that short baroclinic waves may be primarily responsible for EP flux convergence on the poleward side of the climatological jet.

4. Special experiments

To complete the classification of life cycles proposed in section 5, we carry out some special experiments at nearby wavenumbers and with additional basic-state barotropic shear. The life cycle of wavenumber 7 with parameterized latent heat release is qualitatively similar to dry wavenumber 7. We were unable to isolate a moist wavenumber-5 life cycle because of the stronger instability of the wave's subharmonics. We also discuss briefly a wavenumber-8 experiment with explicit water vapor and another with surface friction.

a. Wavenumber-7 life cycle

In Fig. 14b, we saw that a zone of cyclonic barotropic shear is produced during the equilibration of wavenumber 8 life cycle. Wavenumber 6 produces anticyclonic barotropic shear over a broader zone. It is of interest whether there is a smooth transition between these two extreme kinds of equilibration at the intermediate scale, wavenumber 7. We hypothesize that such an equilibration would involve both poleward and equatorward momentum fluxes persisting throughout the life cycle, and that the equilibrated state would have both cyclonic and anticyclonic barotropic shear. That such a state can indeed develop is illustrated in Fig. 19, where we have plotted the eddy momentum fluxes, the deviation of zonal-mean wind, and the EP vectors on day 8 for wavenumber 7.

At this intermediate scale, the normal-mode momentum fluxes (not shown) are entirely equatorward and a low-

TABLE 1. Characteristics of warm core seclusion in baroclinic wave life cycles.

Wavenumber	Innermost secluded contour (K)	Outermost secluded contour (K)	Area inside secluded 280-K contour ($\times 10^{10}$ m^2)	Size of eddy in meridional direction (°)
6 (LC1)	281	270	2.4	50
6 (LC2)	290	264	5.6	48
8	286	274	3.7	33
9	284	274	3.4	27
12	282	276	2.7	24

DAY 3   EP DIAGRAM

Y (DEG, LAT)

DAY 5   EP DIAGRAM
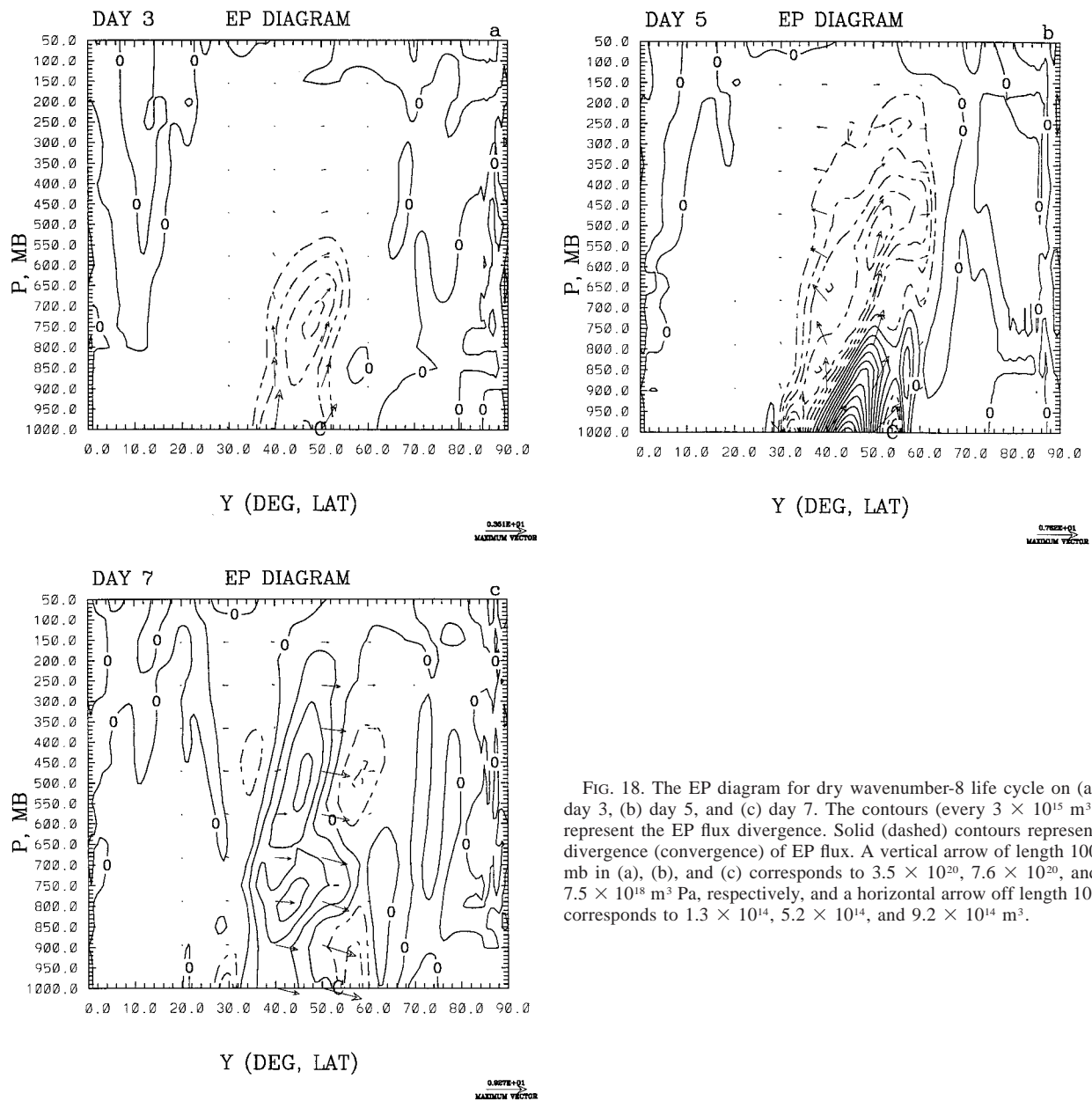

Y (DEG, LAT)

DAY 7   EP DIAGRAM

Y (DEG, LAT)

FIG. 18. The EP diagram for dry wavenumber-8 life cycle on (a) day 3, (b) day 5, and (c) day 7. The contours (every 3×10^{15} m^3) represent the EP flux divergence. Solid (dashed) contours represent divergence (convergence) of EP flux. A vertical arrow of length 100 mb in (a), (b), and (c) corresponds to 3.5×10^{20}, 7.6×10^{20}, and 7.5×10^{18} m^3 Pa, respectively, and a horizontal arrow off length 10° corresponds to 1.3×10^{14}, 5.2×10^{14}, and 9.2×10^{14} m^3.

level easterly jet is accelerated as in wavenumber 8. However, poleward momentum fluxes appear on the southern side of the baroclinic jet as the wave grows. The gradual appearance of poleward fluxes is consistent with the systematic increase in meridional scale, which presumably allows the spherical geometry to influence the dynamics, as discussed in section 3a. The presence of poleward momentum fluxes enhances the low-level westerlies, which migrate poleward as in the life cycle simulation of wavenumber 6 in BG97. At upper levels, poleward momentum fluxes decelerate the flow in the subtropics (Fig. 19b). The EP diagram (Fig. 19c) on day 8 reveals wave radiation to both subtropical and subpolar regions. The downward-

pointing vectors signify equatorward heat fluxes and baroclinic decay on day 8. Feldstein and Held (1989) found radiation to both high and low latitudes during baroclinic life cycles in weakly and moderately supercritical environments using a two-layer QG model.

We used the same basic state to study the dry wavenumber-5 life cycle. The normal mode (not shown) is meridionally broader, but its evolution is very similar to wavenumber 6. The addition of cyclonic barotropic shear (of sinusoidal form with 15 m s^{-1} at 20° and -15 m s^{-1} at 50°) to the basic state results in cyclonic roll up, as at wavenumber 6 (LC2). The cyclonic vortices that appear in the PV analysis at $\theta = 320$ K are much
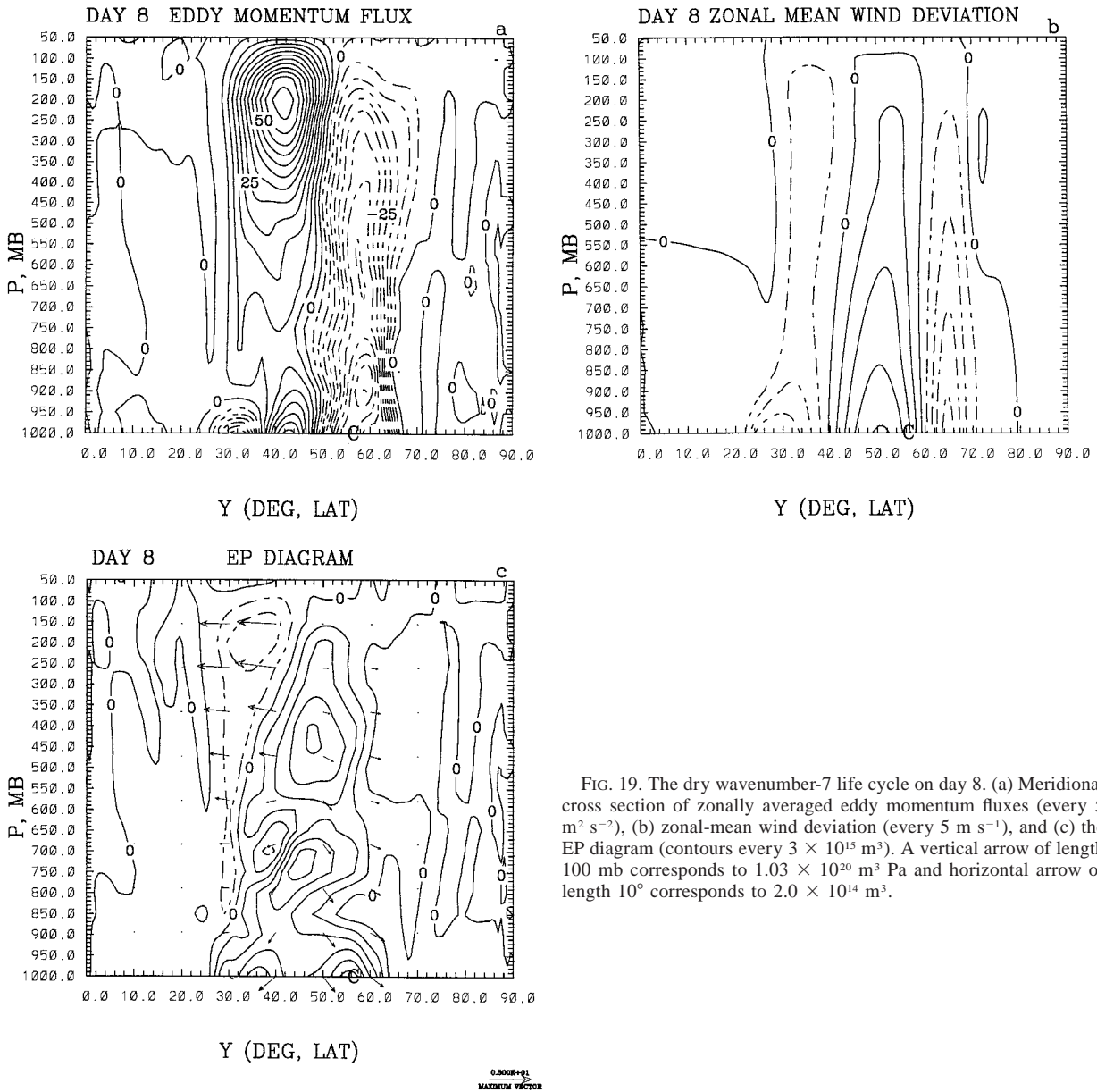
FIG. 19. The dry wavenumber-7 life cycle on day 8. (a) Meridional cross section of zonally averaged eddy momentum fluxes (every 5 $m^2 s^{-2}$), (b) zonal-mean wind deviation (every 5 $m s^{-1}$), and (c) the EP diagram (contours every 3×10^{15} m^3). A vertical arrow of length 100 mb corresponds to 1.03×10^{20} m^3 Pa and horizontal arrow of length 10° corresponds to 2.0×10^{14} m^3.

wider in the meridional direction than the cyclonic vortices at wavenumber 8 (Fig. 8a). Additional cyclonic shear produces only quantitative changes at wavenumber 8 and in shorter waves.

b. Moist wavenumber-8 life cycle with explicit condensation

The latent heat parameterization used so far assumes that all ascent is saturated and all descent is unsaturated. To verify the validity and limitations of the parameterization, we now describe a more realistic moist experiment with explicit water vapor condensation and an initally unsaturated atmosphere. The treatment adds a

prognostic variable for water vapor but does not carry liquid water. Thus, evaporation of rain is still ignored. The relative humidity is a function only of the vertical coordinate σ in the initial state. We use an extrafine resolution of T360 for this experiment. The corresponding gridpoint resolution is about 25 km. Since this scale is small enough to resolve slantwise convection, the relative humidity is chosen such that the initial state is stable to such overturning. The diffusion coefficient is specified to give a decay rate of $(0.25$ h$)^{-1}$ for the shortest scale retained. The dry normal mode for wavenumber 8 with maximum meridional wind of 6 m s^{-1} at the surface is used to initiate the life cycle.

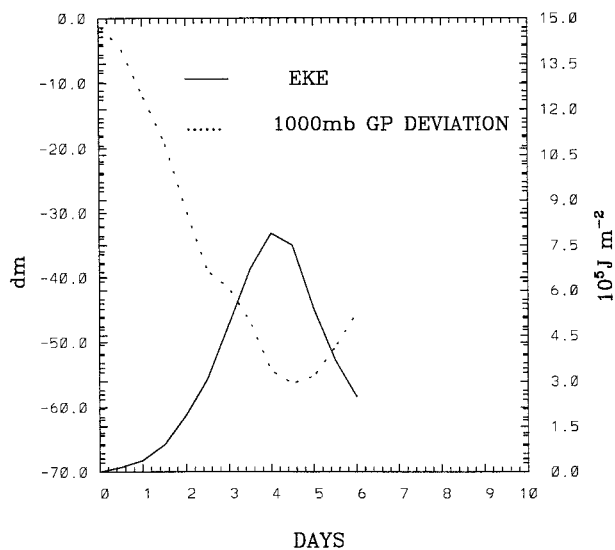The evolution of minimum geopotential deviation at

FIG. 20. The evolution of geopotential deviation at the cyclone center (dashed) and EKE (solid) for moist wavenumber-8 life cycle with explicit condensation scheme.

1000 mb and of the EKE is shown in Fig. 20. The minimum geopotential anomaly occurs on day 4.5 and is much higher than that in the solution with parameterized condensation (Fig. 9a), indicating a weaker spin-up. At the present resolution, convection is not fully resolved and the EKE is probably underestimated as a result. The EKE evolution features 4 days of growth followed by decay. Since the initial disturbance was given more amplitude, the maximum EKE and minimum geopotential deviation are reached a day earlier than in the solution with parameterized condensation. The ''cyclonic'' behavior and the equilibration process

in this solution are similar to the one with with parameterized latent heating.

The explicit representation of condensation and the increased horizontal resolution affect the mesoscale structure of the simulated cyclone. The 1000-mb temperature and geopotential anomaly and the PV field on $\theta = 330$ K on day 3.5 are plotted in Fig. 21. A richer structure can be seen, compared to Fig. 6a. The strengthening of the frontal gradients is mainly due to the higher spatial resolution. There are three centers of warm air near the cyclone center (Fig. 21a). The bent-back warm front has wrapped all the way to the south of the cyclone center. Nearly all of the baroclinicity of the initial state has been confined to a scale of 100–200 km along this front. The long cold front has developed a wavy structure suggesting secondary baroclinic instability at the frontal scale. The upper-level PV fields in the two moist experiments are qualitatively similar (Figs. 8a and 21b), with prominent cyclonic wrapping.

c. Effect of surface friction

To understand the life cycle dynamics in the simplest context, we have so far ignored surface drag and radiative forcing. Since so much of the wave equilibration process is focused at low levels, the omission of surface friction probably has a major impact. The omission of radiative forcing is less problematic, since the radiative restoring timescale in the atmosphere is of the order of a month. The frictional timescale, on the other hand, is closer to one day, much shorter than a typical baroclinic life cycle. Thus, for life cycle studies, the role of radiation can be largely subsumed in the choice of basic state, but surface friction should have a significant direct effect on eddies.
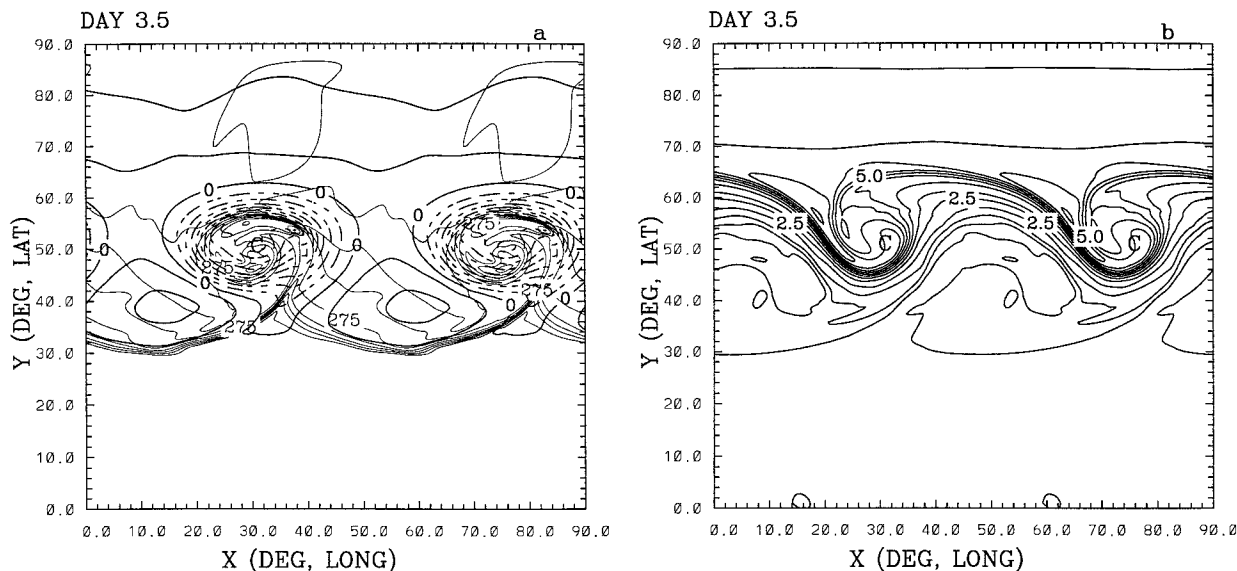

FIG. 21. (a) As in Fig. 5 and (b) as in Fig. 7 but for the moist wavenumber 8 on day 3.5 with explicit condensation.

TABLE 2. Comparison of wavenumber-8 life cycle with and without surface friction.

Characteristic	Control	Friction
Normal mode growth rate	0.76 day^{-1}	0.64 day^{-1}
Normal-mode momentum flux	Equatorward	Equatorward
Max. EKE	4.6×10^5 J m^{-2}	2.9×10^5 J m^{-2}
Max. mean surface easterly	30.0 m s^{-1}	12.9 m s^{-1}
Max. mean surface westerly	27.7 m s^{-1}	10.6 m s^{-1}
Max. upper-level wind on day 10	52.2 m s^{-1}	42.5 m s^{-1}
Equilibration	Cyclonic breaking	Cyclonic breaking

James and Gray (1986) found that in a statistically steady state, the inclusion of surface drag results in greater eddy kinetic energy, owing to the suppression of the barotropic governor. Chang and Orlanski (1993), in their experiments on downstream baroclinic development, found that a small drag coefficient allowed large winds at the surface. However, individual case studies of cyclogenesis (Danard and Ellenton 1980; Orlanski et al. 1991) have shown that an increase in surface drag results in reduced storm intensity.

We conducted a dry wavenumber-8 experiment with surface drag. The linear drag formulation is the same as that used by Held and Suarez (1994), namely,

$$\left(\frac{\partial \mathbf{V}}{\partial t}\right)_{\text{fri}} = -k_v(\sigma)\mathbf{V}, \qquad (9)$$

where $k_v = (1/\tau) \max[0, (\sigma - \sigma_b)/(1 - \sigma_b)]$. The parameters τ and σ_b, respectively, are chosen as 1 day and 0.7, as in Held and Suarez (1994). There is no explicit vertical diffusivity, but the depth of the damping layer is the same as the Ekman depth scale when the vertical diffusivity is roughly 1.1×10^2 m^2 s^{-1}.

In Table 2, we compare the dry wavenumber 8 life cycles with and without surface drag. When surface drag is included, the normal-mode growth rate is reduced and the maximum EKE attained during the life cycle is correspondingly decreased. The normal-mode momentum flux is still equatorward and the final equilibrated state (cf. section 5 and Table 2) is unaltered. However, the barotropic wind created at the surface is drastically reduced and the model atmosphere remains more baroclinic at the end of the life cycle than in the control case. This result is in agreement with the results of James and Gray (1986), who argued that the absence of surface friction allows the creation of large barotropic winds. In their climate simulations, it led to *weaker* EKE over the long term because of the increased zonal-mean horizontal shear.

5. Discussion

The present work is a sequel to BG97, wherein we contrasted the equilibration of wavenumber 6 in Cartesian and spherical geometries. In this study, we have extended the investigation to zonal scales that are more baroclinically active in the presence of condensation. In both studies, we have used energetics and a wave radiation diagnostic (Eliassen–Palm flux) to contrast the different types of equilibration. The present results have been combined with those of BG97 to produce the chart shown in Fig. 22 for the case of symmetric jets. As we have seen here and in BG97, all of these results can be changed by using an *asymmetric* jet with additional cyclonic or anticyclonic horizontal shear.

In addition to zonally symmetric final states, normal-mode experiments produce equilibrated states characterized by axisymmetric, rolled-up eddies. Such a result was obtained by THM by adding a cyclonic barotropic shear to the initial zonal flow, their ''LC2'' experiment. Normal modes in Cartesian geometry also break into trains of robust, cyclonic vortices. However, they decay faster, on a timescale of about one week (BG97). A study by Kida (1981) shows that a barotropic vortex can permanently resist destruction by ambient deformation if its circulation is greater than that of the environment by a certain critical ratio. In the real atmosphere and in forced general circulation models, there is no such sharp distinction between ''permanent'' and ''slowly decaying'' vortices. Thus, the identification of ''LC2'' events in the atmosphere (THM) and in GCMs (Lee and Feldstein 1996) cannot be based solely on long-term behavior. Normal mode experiments artificially remove some of the ambiguity by quantizing the zonal scale.

THM suggest that the longevity of the vortices in cyclonic equilibration is partly due to a region of negative refractive index corresponding to Rossby wave evanescence in the upper troposphere, which limits meridional propagation of wave activity to the subtropics.

TABLE 3. Classification of nonlinear equilibration on the sphere.

| Waves	Zonalizing?	Type of equilibration	Wave radiation toward
Long (wavenumbers 5, 6)	Yes	Anticyclonic breaking	Tropics
Short (8, 9, 10, ...)	Yes	Cyclonic breaking	Poles
Intermediate (7)	Yes	Both types of breaking	Tropics and poles
Long waves with cyclonic barotropic shear	No	Coherent cyclonic vortices	Little radiation

CLASSIFICATION OF BAROCLINIC LIFECYCLES FOR SYMMETRIC JETS
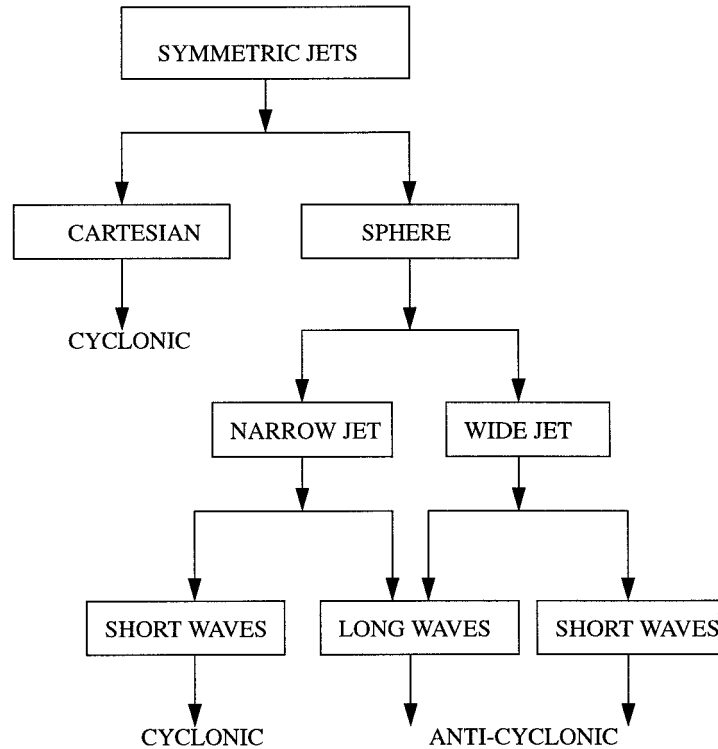
FIG. 22. Chart indicating the type of baroclinic wave equilibration for different geometries and jet characteristics.

However, Lee and Feldstein (1996) do not observe such negative values during episodes of cyclonic roll-up. BG97 also could not find a correlation between refractive index and eddy longevity, and proposed instead that the strength of the barotropic feedback is crucial. However, the present study has shown that short waves (wavenumber 8) zonalize rapidly despite relatively weak barotropic decay. Cutoff vortices form and "shed" their meridional tilt, as in the long-wave roll-up, but these short-wave vortices are not strong enough to resist deformation (zonal elongation) by the ambient flow.

BG97 speculated that a mechanism to symmetrize the vortices rapidly was necessary to avoid complete barotropic decay, but it now appears that the size and strength of the cutoffs must also be considered. To anticipate long-term behavior, one must, it seems, have some measure of the potential strength of the "secluded" anomalies of isentropic PV or surface temperature. This is the kind information that is summarized in Table 1. An even more concise quantity than those in the table is the ratio of the circulation induced by the cutoff to the "ambient" horizontal shear—that is, the part of the shear that is not induced by the cutoff PV and surface temperature features. This ratio is suggested by the results of Kida (1981). A similar measure is the fraction of total perturbation energy that is involved in the induced circulations. Although we certainly have not explored all of the relevant parameter space, the results so far suggest that all of these measures are related to the meridional scale of the normal mode and to the total available baroclinicity.

6. Conclusions

We have investigated wave–mean-flow interaction during the life cycle of short waves on the sphere and the influence of latent heating on these waves, especially their nonlinear equilibration. These "cyclone-scale" waves are important as they bring the "weather" and most of the low-level transience in the midlatitude climate. We have noticed differences between the short and long waves in the wrapping of the warm fronts: the warm front of the short waves wraps cyclonically to form an intense bent-back warm front. In long waves, the anticyclonic shearing by the mean flow is responsible for a less intense bent-back warm front. The secluded warm air (Shapiro and Keyser 1990; BY96) eventually subsides and causes baroclinic decay in short waves. This source of decay is a robust feature of the short waves but is absent from the long waves.

Our experiments with parameterized and explicit condensation schemes demonstrate that explicit condensation

yields much larger amplitudes and shorter timescales than the dry dynamics and brings out the rich mesoscale structure of the waves. By failing to resolve convection on realistic scales, the present solution with explicit moisture still probably underestimates the EKE of an individual baroclinic mode. On the other hand, the solution with parameterized latent heating probably *overestimates* the EKE by failing to remove the convective instability at all. BY96 showed that in a β-plane Cartesian model, the dynamics of the dry and moist cyclones were broadly similar from the point of view of energetics and PV dynamics. Here we have demonstrated that the nature of the equilibration of short waves on the sphere is also fundamentally unaltered by condensation.

Instead of the two paradigms of baroclinic wave life cycles expounded in THM, our results suggest four types of equilibration, summarized in Table 3. Longer baroclinic waves (wavenumbers 4, 5, 6) break anticyclonically on the sphere. The normal modes exhibit a bias toward anticyclonic (SW–NE) tilt and hence predominantly poleward momentum fluxes. During the linear growth period, the poleward momentum-flux convergence moves the low-level westerly jet poleward. The intense feedback between the mean flow and eddy builds anticyclonic zonal-mean flow at a rate that considerably exceeds the linear energy growth rate. In the nonlinear stage, wave activity is radiated meridionally from middle latitudes into the subtropics, mainly at upper levels. The subtropical upper-level mean flow is thereby decelerated and the midlatitudes upper-level flow is accelerated. The final result is a deep layer of anticyclonic meridional shear. Observations of angular momentum transport by eddies (Edmon et al. 1980; Peixoto and Oort 1992) suggest that the atmosphere is dominated by this type of breaking.

As recorded in Table 3, the shorter normal modes (wavenumbers 8, 9, etc.) exhibit a bias toward cyclonic tilt and hence equatorward momentum fluxes. This is similar to the Cartesian modes studied by BG97. Indeed, the higher-wavenumber modes are meridionally confined and do not appear to "feel" sphericity. The equatorward fluxes create a barotropic surface easterly jet poleward of the original jet maximum and the resulting barotropic decay leads to a cyclonic zonal-mean flow in the equilibrated state. In terms of the "saturation-propagation-saturation" (SPS) picture of THM, wave activity is radiated at upper levels into subpolar regions in the nonlinear stage and the cyclonic zonal-mean flow is extended to those levels. Short waves may well be responsible for the convergence of wave activity near 50° at upper levels in climatological data (Edmon et al. 1980) and in GCMs (Lee and Feldstein 1996). Moist short-wave solutions are similar, but there is more intense warm frontogenesis and cyclonic wrapping of PV contours. The differences in life cycle behavior attributed to model geometry in Whitaker and Snyder (1993) and BG97 are virtually absent in short waves.

Interestingly, the wavenumber 7 life cycle possesses both types of behavior, suggesting a smooth transition from mainly anticyclonic to mainly cyclonic breaking as the wavenumber increases. The momentum fluxes converge at midlatitudes throughout the life cycle. The equilibrated mean flow has barotropic westerlies at the center and easterlies in the subtropical and subpolar regions. The evolution of the flow is similar to that in a QG β-plane model with a symmetric initial jet (Nakamura 1993). The EP diagram in the nonlinear stage indicates wave radiation to both subtropical and subpolar regions.

Long waves with equatorward momentum fluxes during the linear stage (LC2 of THM) exhibit cyclonic roll-up in the nonlinear stage. BG97 found that the feedback between the momentum fluxes and zonal-mean wind shuts down early in long waves if the waves have cyclonic tilt during the linear stage. In the absence of strong barotropic shear, a large amount of warm air may break off to form coherent vortices, provided the zonal scale allows the temperature contrast across the jet to be fully tapped. A sufficiently strong vortex can symmetrize by shedding filaments *and* resist deformation by the ambient flow.

Previous studies (e.g., Simmons and Hoskins 1978) have contrasted eddy momentum fluxes of short and long baroclinic waves. We have attempted to relate the direction of the fluxes both to the linear mode and to the type of wave breaking. The results may have implications for eddy momentum, heat, and PV flux parameterizations in low-resolution GCMs of the atmosphere and ocean. In particular, the sensitivity of the eddy fluxes to zonal scale and "ambient" shear is a potential practical complication for closure theories based on the strength of the ambient baroclinicity (e.g., Pavan and Held 1996) and an assumption of a homogeneous environment (e.g., Held and Larichev 1996).

The main limitation of this work, namely, the restriction of the basic states to idealized zonally symmetric mean flow and normal modes, prevents the direct application of the results to the real climate. Midlatitude disturbances are typically organized into baroclinic wave packets rather than a uniform wave train consisting of single wavenumber (Lee and Held 1993; Chang and Orlanski 1993). Other important physical processes like surface heat and moisture fluxes, evaporation, cloud microphysics, radiation, interaction with topography, and surface drag have been omitted. The relevance of normal-mode eddy momentum fluxes of long and short baroclinic waves in a statistically steady climate will be the subject of a future paper.

REFERENCES

Balasubramanian, G., and M. K. Yau, 1994a: Baroclinic instability in a two layer model with parameterized slantwise convection. *J. Atmos. Sci.,* **51,** 971–990.

——, and ——, 1994b: The effects of convection on a simulated marine cyclone. *J. Atmos. Sci.,* **51,** 2397–2417.

——, and ——, 1996: The life cycle of a simulated marine cyclone: Energetics and PV diagnostics. *J. Atmos. Sci.,* **53,** 639–653.

——, and S. T. Garner, 1997: The role of eddy momentum fluxes in shaping the life cycle of a baroclinic wave. *J. Atmos. Sci.,* **54,** 510–533.

Bourke, W., 1974: A multilevel spectral model. Part I: Formulation and hemispheric integrations. *Mon. Wea. Rev.,* **102,** 687–701.

Chang, K. M., and I. Orlanski, 1993: On the dynamics of a storm track. *J. Atmos. Sci.,* **50,** 999–1015.

Danard, M. B., 1964: On the influence of released latent heat on cyclone development. *J. Appl. Meteor.,* **3,** 27–37.

——, and G. E. Ellenton, 1980: Physical influences on east coast cyclogenesis. *Atmos.-Ocean,* **18,** 65–82.

Davis, C. A., and K. A. Emanuel, 1991: Potential vorticity diagnostics of cyclogenesis. *Mon. Wea. Rev.,* **119,** 1929–1953.

Edmon, H. J., B. J. Hoskins, and M. E. McIntyre, 1980: Eliassen–Palm cross sections for the troposphere. *J. Atmos. Sci.,* **37,** 2600–2616.

Emanuel, K. A., M. Fantini, and A. J. Thorpe, 1987: Baroclinic instability in an environment of small stability to slantwise moist convection. *J. Atmos. Sci.,* **44,** 1559–1573.

Fantini, M., 1991: Baroclinic instability and induced air-heat exchange. *Tellus,* **43A,** 285–294.

——, 1995: Moist Eady waves in a quasigeostrophic three-dimensional model. *J. Atmos. Sci.,* **52,** 2473–2485.

Feldstein, S. B., and I. M. Held, 1989: Barotropic decay of baroclinic waves in a two-layer beta plane model. *J. Atmos. Sci.,* **46,** 3416–3430.

Gall, R. L., 1976: The effects of released latent heat in growing baroclinic waves. *J. Atmos. Sci.,* **33,** 1686–1701.

Gutowski, W. J., L. E. Bronscome, and D. S. Stewart, 1992: Life cycles of moist baroclinic eddies. *J. Atmos. Sci.,* **49,** 306–319.

Gyakum, J. R., 1983a: On the evolution of the *QE II* storm. Part I: Synoptic aspects. *Mon. Wea. Rev.,* **111,** 1137–1135.

——, 1983b: On the evolution of the *QE II* storm. Part II: Dynamic and thermodynamic structure. *Mon. Wea. Rev.,* **111,** 1156–1173.

Hedley, M., and M. K. Yau, 1991: Anelastic modeling of explosive cyclogenesis. *J. Atmos. Sci.,* **48,** 711–727.

Held, I. M., and B. J. Hoskins, 1985: Large scale eddies and the general circulation of the troposphere. *Advances in Geophysics,* Vol. 28A, Academic Press, 3–31.

——, and M. J. Suarez, 1994: A proposal for the intercomparison of the dynamical cores of atmospheric general circulation models. *Bull. Amer. Meteor. Soc.,* **75,** 1825–1835.

——, and V. D. Lavichev, 1996: A scaling theory for horizontally homogeneous baroclinically unstable flow on a beta plane. *J. Atmos. Sci.,* **53,** 946–956.

Holton, J. R., 1992: *An Introduction to Dynamic Meteorology.* 3d ed. Academic Press, 511 pp.

Hoskins, B. J., M. E. McIntyre, and A. W. Robertson, 1985: On the use and significance of isentropic potential vorticity maps. *Quart. J. Roy. Meteor. Soc.,* **111,** 877–946.

James, I. N., 1987: Suppression of baroclinic instability in horizontally sheared flows. *J. Atmos. Sci.,* **44,** 3710–3720.

——, and L. J. Gray, 1986: Concerning the effect of surface drag on the circulation of a baroclinic planetary atmosphere. *Quart. J. Roy. Meteor. Soc.,* **112,** 1231–1250.

Joly, A., and A. J. Thorpe, 1991: Warm and occluded fronts in two dimensional moist baroclinic instability. *Quart. J. Roy. Meteor. Soc.,* **115,** 513–534.

Kida, S., 1981: Motion of an elliptic vortex in a uniform shear flow. *J. Phys. Soc. Japan,* **50,** 3517–3520.

Kuo, Y. H., M. A. Shapiro, and E. G. Donall, 1991: The interaction between baroclinic and diabatic processes in a numerical simulation of a rapidly intensifying marine cyclone. *Mon. Wea. Rev.,* **119,** 457–476.

Lee, S., and I. M. Held, 1993: Baroclinic wave packets in models and observations. *J. Atmos. Sci.,* **50,** 1413–1428.

——, and S. Feldstein, 1996: Two types of wave breaking in an aquaplanet GCM. *J. Atmos. Sci.,* **53,** 842–856.

Montgomery, M. T., and B. F. Farrell, 1991: Moist surface frontogenesis associated with interior potential vorticity anomalies in a semigeostrophic model. *J. Atmos. Sci.,* **48,** 2484–2505.

Nakamura, H., 1992: Midwinter suppression of baroclinic wave activity in the Pacific. *J. Atmos. Sci.,* **49,** 1629–1642.

——, 1993: Momentum flux, flow symmetry, and the nonlinear barotropic governor. *J. Atmos. Sci.,* **50,** 2159–2179.

Neiman, P. J., and M. A. Shapiro, 1993a: The life cycle of an extratropical cyclone. Part I: Frontal evolution and thermodynamic air–sea interaction. *Mon. Wea. Rev.,* **121,** 2153–2176.

——, and ——, 1993b: The life cycle of an extra-tropical cyclone. Part II: Mesoscale structure and diagnostics. *Mon. Wea. Rev.,* **121,** 2177–2199.

Orlanski, I., and J. Katzfey, 1987: Sensitivity of model simulations for a coastal cyclone. *Mon. Wea. Rev.,* **115,** 2792–2821.

——, ——, C. Menendez, and M. Marino, 1991: Simulation of an extratropical cyclone in the Southern Hemisphere: Model sensitivity. *J. Atmos. Sci.,* **48,** 2293–2311.

Paran, V., and I. M. Held, 1996: The diffusive approximation for eddy fluxes in baroclinically unstable jets. *J. Atmos. Sci.,* **53,** 1262–1272.

Parker, D. J., and A. J. Thorpe, 1995: Conditional convective heating in a baroclinic atmosphere. A model of convective frontogenesis. *J. Atmos. Sci.,* **52,** 1699–1711.

Peixoto, J. P., and A. H. Oort, 1992: *Physics of Climate.* American Institute of Physics, 520 pp.

Randel, W. J., and J. L. Stanford, 1985: The observed life cycle of a baroclinic instability. *J. Atmos. Sci.,* **42,** 1364–1373.

——, and I. M. Held, 1991: Phase speed spectra of transient eddy fluxes and critical layer absorption. *J. Atmos. Sci.,* **48,** 688–697.

Robert, A. F., 1966: The integration of a low order spectral form of the primitive meteorological equations. *J. Meteor. Soc. Japan,* **44,** 237–245.

Shapiro, M. A., and D. Keyser, 1990: Fronts, jet streams and the tropopause. *Extratropical Cyclones: The Erik Palmén Memorial Volume,* C. W. Newton and E. O. Holopainen, Eds., Amer. Meteor. Soc., 262 pp.

Simmons, A. J., and B. J. Hoskins, 1976: Baroclinic instability on the sphere: Normal modes of the primitive and quasi-geostrophic equations. *J. Atmos. Sci.,* **33,** 1454–1477.

——, and ——, 1978: The life cycles of some nonlinear baroclinic waves. *J. Atmos. Sci.,* **35,** 414–432.

Snyder, C., W. C. Skamarock, and R. Rotunno, 1991: A comparison of primitive-equation and semigeostrophic simulations of baroclinic waves. *J. Atmos. Sci.,* **48,** 2179–2194.

Thorncroft, C. D., B. J. Hoskins, and M. E. McIntyre, 1993: Two paradigms of baroclinic wave life cycle behavior. *Quart. J. Roy. Meteor. Soc.,* **119,** 17–55.

Thorpe, A. J., and K. A. Emanuel, 1985: Frontogenesis in the presence of small moist symmetric stability. *J. Atmos. Sci.,* **42,** 1809–1824.

Tracton, M. S., 1973: The role of cumulus convection in the development of extratropical cyclone. *Mon. Wea. Rev.,* **101,** 573–593.

Wang, B., and A. Barcilon, 1986: Moist stability of a baroclinic zonal flow with conditionally unstable stratification. *J. Atmos. Sci.,* **43,** 705–719.

Whitaker, J. S., and C. Snyder, 1993: The effects of spherical geometry on the evolution of baroclinic waves. *J. Atmos. Sci.,* **50,** 597–612.

——, and C. A. Davis, 1994: Cyclogenesis in a saturated environment. *J. Atmos. Sci.,* **51,** 889–907.